PHYSICAL REVIEW D **86,** 064008 (2012)

Three-dimensional evolution of differentially rotating magnetized neutron stars

Kenta Kiuchi,[1] Koutarou Kyutoku,[1,2] and Masaru Shibata[1]

[1]*Yukawa Institute for Theoretical Physics, Kyoto University, Kyoto, 606-8502, Japan*

[2]*Theory Center, Institute of Particles and Nuclear Studies, KEK, Tsukuba, Ibaraki, 305-0801, Japan*

(Received 29 May 2012; published 4 September 2012)

We construct a new three-dimensional general relativistic magnetohydrodynamics code, in which a fixed mesh refinement technique is implemented. To ensure the divergence-free condition as well as the magnetic flux conservation, we employ the method by Balsara [J. Comp. Physiol. **174**, 614 (2001); J. Comp. Phys. **228**, 5040 (2009)]. Using this new code, we evolve differentially rotating magnetized neutron stars, and find that a magnetically driven outflow is launched from the star exhibiting a kink instability. The matter ejection rate and Poynting flux are still consistent with our previous finding [M. Shibata, Y. Suwa, K. Kiuchi, and K. Ioka, Astrophys. J. **734**, L36 (2011)] obtained in axisymmetric simulations.

DOI: 10.1103/PhysRevD.86.064008 PACS numbers: 04.25.D−, 04.30.−w, 04.40.Dg

I. INTRODUCTION

Ground-based gravitational-wave detectors, Advanced LIGO, Advanced VIRGO, and KAGRA will be in operation in the next five years [1]. The first observation of gravitational waves, thus, will be achieved in the near future. Among their sources of gravitational waves, coalescence of binary neutron stars (BNS) is the most promising one, and the detection of gravitational waves from them will provide us unique information of strongly gravitational fields and properties of dense nuclear matter. The BNS merger is also the potential candidate for the progenitor of short-hard gamma-ray bursts [2]. For the theoretical studies of the BNS mergers, numerical relativity is the unique and robust approach. A number of numerical simulations have been performed [3–19] since the first success in 2000 [20].

Magnetic fields could play an important role in BNS mergers because the inferred value of the magnetic-field strength via the observed spin period P and their time derivative $\dot{P}$ is high as 10^{11}–10^{14} G for radio pulsars, of which more than 1800 are known to date [21]. During the merger process, several mechanisms such as compression, magnetic winding, and magnetorotational instability (MRI) [22] could amplify their magnetic-field strength. This amplified magnetic field could have an impact on the dynamics of the mergers because it contributes to the angular momentum transport and the magnetic pressure may modify the structure of the objects formed after the merger. Motivated by this expectation, several groups have implemented the magnetohydrodynamics (MHD) code in the framework of numerical relativity [23–28]. These numerical codes developed have been applied to collapse of magnetized hypermassive neutron stars (HMNS) [29–31], magnetized neutron star-black hole binary merger [32,33], evolution of magnetized neutron stars [34–36], and magnetorotational collapse of massive stellar cores [24,37].

In the context of BNS mergers, several groups have assessed what the role of magnetic fields is during the inspiral and merger [38–42]. Their findings are summarized as follows: As long as the magnetic-field strength before the merger is not unrealistically large, e.g., 10^{16}–10^{17} G, the magnetic field does not give a strong impact on the inspiral dynamics. When the external layers of the two neutron stars come into contact, the Kelvin-Helmholtz instability develops and forms vortexes. Poloidal magnetic-field lines are curled by them and generate a toroidal field in a short time scale. The saturation point of the magnetic-field strength is still under debate because the field strength found in Ref. [40] is not as high as found in Ref. [43]. If the total mass of BNS is large enough to collapse to a black hole surrounded by a torus, the magnetic field in the torus may be subject to the MRI [41]. On the other hand, if the total mass is not large enough, a long-lived HMNS [44] is born and the magnetic-field amplification would be realized inside the HMNS. The later case has not been explored in detail, because high computational costs for a longterm well-resolved simulation prevent this study.

The recent measurement of mass for PSR J1614-2230 ($M_{J1916\text{-}2230} = 1.97 \pm 0.04 M_\odot$) [45] gave a strong constraint on nuclear equations of state (EOS). Together with the fact that the canonical observed mass of neutron stars is 1.3–$1.4 M_\odot$, it is natural to infer that a long-lived HMNS will be born in the merger of BNS composed of neutron stars with the canonical mass [9]. This implies that it is mandatory to perform a long-term and high-resolution simulation of magnetized BNS mergers.

In Ref. [35], we have developed a three-dimensional general relativistic magnetohydrodynamics (GRMHD) code, which has an uni-grid structure with fish-eye coordinates. The dynamical range of the BNS system is quite large spanning from the neutron-star size to the wave length of gravitational waves. Thus, we should implement

a mesh refinement technique to save computational costs. In the framework of GRMHD, the implementation of mesh refinement techniques has been done in three methods. For all the approaches, a special care for preserving the divergence-free condition of magnetic fields is taken. In the first approach, equations for vector potentials instead of magnetic fields are solved. In this method, any unconstrained interpolations in the refinement boundaries, where the boundary condition for child domains are determined using the data of their parent domains, may be allowed for preserving the divergence-free condition of magnetic fields [40,46,47]. In the second approach, the hyperbolic divergence-cleaning prescription is employed to ensure the divergence-free condition of magnetic fields [26,42]. The third one [24] is based on the Balsara's constrained-transport scheme, in which a special interpolation scheme in the refinement boundaries is mandatory to preserve the divergence-free condition and *the magnetic-flux conservation* [48,49]. We construct a new GRMHD code employing the third approach (modifying the original scheme for the use in the vertex-centered grid) to precisely guarantee the divergence-free condition and the magnetic-flux conservation. It is worthy to note that this method is likely to work well also in the presence of a black hole.

As the first application of our new code, we extend our previous work in Ref. [36], in which an axisymmetric HMNS with magnetic fields was evolved. In that work, we found that a mildly relativistic outflow is driven from the HMNS accompanying a strong Poynting flux of magnitude proportional to $B^2R^3\Omega$ (where B, R, and Ω denote the typical magnitudes of the magnetic field, radius, and angular velocity of the HMNS) emitted toward the direction of the rotational direction. However, it was not clear that three-dimensional effects, in particular the effect of nonaxisymmetric instabilities such as kink instability [50], would not play a role in this phenomenon. For a more physical study, we obviously had to perform a three-dimensional simulation.

The paper is organized as follows: In Sec. II, the formulation to solve Einstein's equations as well as GRMHD equations are briefly summarized. In addition, we briefly describe a method to implement the fixed mesh refinement (FMR) algorithm in particular for magnetic fields, and also mention the initial condition and grid setup. In Sec. III, we present numerical results for the evolution of a rapidly rotating magnetized neutron star, focusing on the properties of the material and Poynting flux ejected from it. Section IV is devoted to discussing the implication of our numerical results and a summary of this paper. In the Appendices, our method for implementing the FMR scheme and results for the several standard test-bed simulations are shown. Throughout this paper, Greek and Latin indices denote the spacetime and spatial components, respectively.

II. FORMULATION, METHOD AND MODEL

A. Formulation and numerical issue

We study the evolution of a rapidly rotating magnetized neutron star by a three-dimensional GRMHD simulation in the framework of ideal MHD. The formulation and numerical scheme for solving Einstein's equations are the same as in Ref. [35], in which one of the Baumgarte-Shapiro-Shibata-Nakamura (BSSN) formulations [51–54] is employed, and a fourth-order finite-differencing scheme in the spatial direction and a fourth-order Runge-Kutta scheme in the time integration are implemented. The advection terms in Einstein's evolution equations are evaluated with a fourth-order lopsided finite-differencing scheme, as, e.g., in Ref. [55]. A conservative shock-capturing scheme is employed to integrate GRMHD equations. Specifically, we use a high resolution central scheme [56] with the third-order piece-wise parabolic interpolation and a steep min-mod limiter.

We implement a FMR algorithm to our original three-dimensional GRMHD code [35] which has an uni-grid structure with fish-eye coordinates [57]. Our FMR scheme is essentially the same as an adaptive-mesh refinement (AMR) scheme of SACRA [6], and enables us to assign fine grids in the vicinities of neutron stars or black holes, while enlarging the computational domain which covers a local wave zone of gravitational waves with less computational cost. The schemes for solving Einstein's equations and hydrodynamics equations (the continuity, momentum, and energy equations) are also the same as those of SACRA code [6], in which geometric variables and fluid variables (density, pressure, internal energy, specific momentum, and specific energy) are placed at the vertex-centered grids and the grid spacing of a ''parent'' domain is twice as large as that of its ''child'' domain. Each domain is equally composed of $(2N+1, 2N+1, 2N+1)$ Cartesian grid zones for (x, y, z), each of which covers the interval $[-N\Delta x_l, N\Delta x_l]$ for the x-, y- and z-directions with Δx_l being the grid spacing of the lth FMR level. The label l varies from 1 (for the coarsest and largest domain) to $l_{\rm max}$ (for the finest and smallest one). The prolongation, i.e., interpolation from a ''parent'' domain to a ''child'' domain, of the geometric and fluid variables in the refinement boundaries are done with a fifth-order Lagrange interpolation. Because our grid is located at the vertex centers, the restriction procedure, i.e., interpolation from a ''child'' domain to a ''parent'' domain, is straightforwardly done, by simply copying the data from a child domain to its parent domain.

On the other hand, for integrating the induction equation, we need a special care to preserve the divergence-free condition of magnetic fields and to guarantee the magnetic-flux conservation. For this purpose, several GRMHD codes constructed so far [25,27,28,46] have implemented either the constrained-transport (CT) [58] or flux-CT scheme [59]. In the code of implementing FMR or AMR algorithm,

we are required to take an additionally special care when performing the prolongation and restriction procedures of magnetic fields in the refinement boundaries, as described in Refs. [46–49]. AMR-GRMHD codes of Refs. [40,46] exploited a method of evolving the vector potential. This method guarantees the preservation of the divergence-free condition for magnetic fields avoiding complex interpolation procedures in the refinement boundaries. However, *this method does not guarantee the magnetic-flux conservation* in the refinement boundaries, because the magnetic fields are calculated by a finite differencing of the vector potential and this procedure does not in general guarantee the magnetic-flux conservation.

Alternatively, the AMR-GRMHD code of Ref. [26] employs a hyperbolic divergence-cleaning technique [60]. In this scheme, a scalar field is introduced, which is coupled to the system of the MHD and induction equations. No special prescription is needed for the finite differencing when solving GRMHD equations, and a nonzero divergence of magnetic fields either propagates or damps away when they are spuriously excited. However, as mentioned in Ref. [46], this method is likely to be incompatible with the moving puncture method [53,54], which is commonly used to evolve black-hole spacetimes in the Baumgarte-Shapiro-Shibata-Nakamura formulations.

The AMR-GRMHD code in Ref. [24] implements the flux-CT scheme for magnetic fields. In this scheme, both the preservation of the divergence-free condition and the magnetic-flux conservation are guaranteed in the refinement boundaries in the machine precision level. However, the code of Ref. [24] is second-order accurate both in space and in time. We have developed a new code, which is based on the flux-CT scheme (i.e., which can ensure the magnetic-flux conservation and the divergence-free condition in the refinement boundaries), and which is fourth-order accurate in time. Following the method described in Refs. [48,49], we employ a divergence-free-preserving interpolation based on WENO5 [61]. In Appendix A, the grid structure, the scheme for integrating the induction equation, as well as the prolongation/restriction schemes of magnetic fields are described in details. Results for several test-bed simulations in Appendix B illustrate the reliability of our new code.

B. Initial condition, density atmosphere and grid setup

Following Refs. [30,36], we adopt a rapidly and differentially rotating neutron star in an axisymmetric equilibrium as the initial conditions. It is a model of the HMNS formed after the merger of a BNS. To model the neutron star, the following piecewise polytropic EOS composed of two pieces is employed:

$$P_{\rm cold} = \begin{cases} K_1 \rho^{\Gamma_1} & (\rho \le \rho_{\rm nuc}), \\ K_2 \rho^{\Gamma_2} & (\rho \ge \rho_{\rm nuc}). \end{cases} \tag{2.1}$$

Here, P and ρ are the pressure and rest-mass density, respectively. The specific internal energy, ε, is derived assuming the first law of thermodynamics $d\varepsilon = -Pd(1/\rho)$, and this specific internal energy written as a function of ρ is referred to as $\varepsilon_{\rm cold}$ (i.e., we initially set $\varepsilon = \varepsilon_{\rm cold}(\rho)$). Following Ref. [30], the parameters are chosen to be $\Gamma_1 = 1.3$, $\Gamma_2 = 2.75$, $K_1 = 5.16 \times 10^{14}$ cgs, $K_2 = K_1 \rho_{\rm nuc}^{\Gamma_1 - \Gamma_2}$, and $\rho_{\rm nuc} = 1.8 \times 10^{14}$ g/cm^3. This EOS produces spherical neutron stars whose maximum gravitational mass $M_{\rm max}$ (rest mass $M_{\rm b,max}$) is $2.01 M_\odot$ ($2.32 M_\odot$) and rigidly rotating neutron stars with $M_{\rm max}(M_{\rm b,max}) = 2.27 M_\odot (2.60 M_\odot)$. For the rotational law, we assume the same profile as employed in Refs. [30,36]. Table I shows the parameters of the differentially rotating neutron-star model which we adopt.

During the simulations, we use a hybrid EOS as $P = P_{\rm cold} + (\Gamma_{\rm th} - 1)\rho(\varepsilon - \varepsilon_{\rm cold})$ with $\Gamma_{\rm th} = \Gamma_1$. Our choice of $\Gamma_{\rm th}$ may be rather small. We choose this small value to focus on the mass ejection from the rotating neutron star primarily by the magnetorotational effects suppressing shock heating effects.

A dipole magnetic field is superimposed initially. We assume that the axis of the dipole is aligned with the rotation axis as in the previous paper [36], and write the vector potential in the form

$$A_\varphi = \frac{A_0 \varpi_0^2}{(R^2 + z^2 + \varpi_0^2)^{3/2}}, \tag{2.2}$$

where we used the cylindrical coordinate (R, z, φ). ϖ_0 is set to be $10/3 R_{\rm e}$ with $R_{\rm e}$ being the equatorial stellar radius. A_0 determines the magnetic-field strength and we adjust this parameter to achieve the maximum field strength B_0 to be 4.2×10^{13} G and 1.7×10^{14} G. According to the magnetic-field strength, we refer to these models as B13 and B14, respectively. Here, B_0 is defined by $B \equiv \sqrt{b^\mu b_\mu}$ where b^μ is the four-vector of the magnetic field in the fluid rest frame.

We note that there is no reason to believe that the dipole axis is aligned with the rotation axis for the HMNS formed after a BNS merger. The reason for our choice of this simple profile is that the purpose of this paper is to compare the results in three-dimensional simulations with those in the axisymmetric one performed in Ref. [36]. If the axes of the dipole and rotation do not align with each other, the mechanism for the amplification of the magnetic field and

TABLE I. Physical parameters of a differentially rotating neutron star employed: Gravitational mass M, baryon rest mass M_b, central density (maximum density) $\rho_{\rm max}$, angular momentum cJ/GM^2, central rotation period P_c, and coordinate radius on the equator $R_{\rm e}$.

$M(M_\odot)$	$M_b(M_\odot)$	$\rho_{\rm max}$(g/cm^3)	cJ/GM^2	P_c (ms)	$R_{\rm e}$ (km)
2.02	2.23	9.49×10^{14}	0.66	0.48	11.4

TABLE II. Model parameters and grid setup: Maximum strength for the initial dipole magnetic field B_0, the finest grid resolution $\Delta x_{l_{\max}}$, the grid point within one refinement domain N, the total number of FMR domains $l_{\max}$, the location of the outer boundary L_0 along each axis, and the assumption for the equatorial plane symmetry.

Model	B_0 [G]	$\Delta x_{l_{\max}}$ [km]	N	$l_{\max}$	L_0 [km]	eq-symmetry
B14	1.7×10^{14}	0.142	96	8	1740	yes
B13	4.2×10^{13}	0.142	96	8	1740	yes
B13L	4.2×10^{13}	0.190	72	8	1740	yes
B14F	1.7×10^{14}	0.142	96	8	1740	no

subsequent dynamical process of the system could be significantly modified. We will perform more systematic studies varying the axis direction of the dipole in the future work.

As discussed in Ref. [36], a tenuous density atmosphere has to be put outside the neutron star for stably evolving magnetically driven outflows. If the atmosphere is dense, the outflow and magnetic-field profile are substantially affected by the inertia of the atmosphere. Thus, we have to set the density of the atmosphere to be as low as possible. Specifically, we set it as

$$\rho_{\rm at} = \begin{cases} f_{\rm at}\rho_{\max} & (r \le 2R_{\rm e}), \\ f_{\rm at}\rho_{\max}(r/2R_{\rm e})^{-n} & (r \ge 2R_{\rm e}), \end{cases} \tag{2.3}$$

where $\rho_{\max}$ denotes the maximum rest-mass density of the neutron star. We set $f_{\rm at} = 10^{-9}$ and $n = 2$. As long as we use these values, the magnetic field evolution depends only weakly on the atmosphere [36].

Table II summarizes the dipole field strength and grid setup. The stars are contained in the numerical domain composed of the finest grid resolution. In the typical simulations, $R_{\rm e}$ is covered by 80 grid points in the finest domain. The side length in one positive direction of the finest domain is $1.2R_{\rm e}$. We prepare 8 refinement domains and in this case, the outer boundary is located at $\approx 150R_{\rm e}$. For models B13 and B14, the simulations were performed in this grid setup. To confirm the convergence of numerical results, we also performed a simulation for the low-resolution model B13L, in which $R_{\rm e}$ is covered by 60 grid points in the finest domain, while keeping the outer boundary at the same position as the high resolution model. In these three models, the equatorial plane symmetry is imposed. We also performed a simulation for model B14F for which no symmetry is assumed. This simulation is devoted to exploring the dependence of the symmetry effect on the evolution of the magnetized neutron stars.

III. NUMERICAL RESULTS

A. Prediction

First, we summarize the predicted numerical results based on the findings of Ref. [36], and then, describe three-dimensional effects that are not taken into account in the previous work [36]. In the present setup, the magnetic winding due to the presence of differential rotation and poloidal magnetic fields will take place and then, a strong toroidal field will be generated [62]. The magnitude of the toroidal magnetic field increases linearly with time during the winding. In particular, a strong magnetic field is generated near the rotation axis. After the substantial winding, the magnetic pressure associated with the strong toroidal field overcomes the gravitational binding energy in the vicinity of the neutron-star polar surface. Then, a sub- or mildly relativistic outflow will be launched primarily toward the direction perpendicular to the equatorial plane. In the outflow, both a matter outflow and a Poynting flux are generated. The magnitudes of the luminosity for these would be [36]

$$L_M \sim 10^{48}\left(\frac{B_0}{10^{13}\,{\rm G}}\right)^2\left(\frac{R_{\rm e}}{10^6\,{\rm cm}}\right)^3\left(\frac{\Omega}{10^4\,{\rm rad/s}}\right){\rm ergs/s}, \tag{3.1}$$

$$L_B \sim 10^{47}\left(\frac{B_0}{10^{13}\,{\rm G}}\right)^2\left(\frac{R_{\rm e}}{10^6\,{\rm cm}}\right)^3\left(\frac{\Omega}{10^4\,{\rm rad/s}}\right){\rm ergs/s}, \tag{3.2}$$

where Ω is the typical magnitude of the angular velocity. Here, L_M includes the contribution of the rest-mass energy flow, and thus, the luminosity for the kinetic energy would be by about two orders of magnitude smaller for the outflow velocity $\sim$0.1–0.2 c.

The simulations of Ref. [36] were performed assuming the axial symmetry. In the nonaxisymmetric case, we should consider that the nonaxisymmetric kink instability [50] could turn on because the outflow contains a strong toroidal field generated by the winding as a dominant magnetic-field component. Reference [63] indeed showed that the kink instability turns on in a magnetically driven jet from a black hole-torus system, if it has a strong toroidal field. In the following, we will show a numerical result which illustrates that the kink instability indeed turns on. The question is how the effect of this instability modifies the results of the axisymmetric simulations [36].

B. Properties of outflow

Figure 1 plots the evolution of the electromagnetic energy as a function of time for all the models employed in this paper. We define the electromagnetic energy by

$$E_B = \frac{1}{8\pi}\int b^2 w\sqrt{\gamma}{\rm d}^3x, \tag{3.3}$$

where γ is the determinant of the spatial metric and $w = -n_\mu u^\mu$ with n^μ being a timelike unit vector normal to the spatial hypersurface and u^μ being a four velocity. E_B is decomposed into the poloidal component $E_{\rm P}$ and toroidal one $E_{\rm T}$ as

$$E_{\rm P} = \frac{1}{8\pi}\int (b^R b_R + b^z b_z) w\sqrt{\gamma}{\rm d}^3x, \tag{3.4}$$

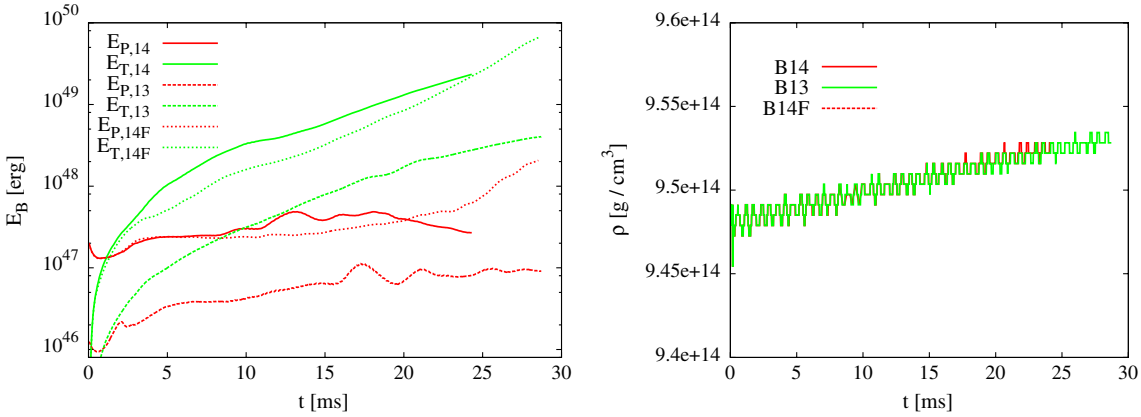

FIG. 1 (color online). (Left) Evolution of the poloidal-field energy $E_{\rm P}$ and toroidal-field energy $E_{\rm T}$ for three models B14, B13, and B14F, labeled by "14", "13", and "14F", respectively. (Right) Evolution of the central rest-mass density.

$$E_{\rm T} = \frac{1}{8\pi}\int b^{\varphi} b_{\varphi} w\sqrt{\gamma}\,{\rm d}^3x. \tag{3.5}$$

As expected, the toroidal-field energy for all the models increases with time due to the magnetic winding. In a relatively short time scale $\sim$1 ms ($\approx 2P_c$), the toroidal-field energy catches up with the poloidal one, and then, it becomes the dominant component. We find the growth rate of the toroidal field is consistent with the winding mechanism, in which the toroidal field $B_{\rm T}$ should increase in proportional to $\sim B_{\rm P}\Omega t$ with $B_{\rm P}$ being the poloidal magnetic field.

The toroidal-field energy for model B14F starts deviating from that for model B14 at $t \sim 3$ ms and the growth rate for model B14F is slightly smaller than that for model B14. On the other hand, for $t \gtrsim 24$ ms, the toroidal-field energy for model B14F overcomes that for model B14. These facts imply that an asymmetry with respect to the equatorial plane comes into the play in the amplification process of the magnetic field (see also the left panel of Fig. 3), although this effect does not change the amplification process qualitatively and significantly.

For all the models, the poloidal-field energy also changes with time, and is eventually larger than the initial value by a factor of $\sim$2–10. If the system is axisymmetric, the poloidal-field energy changes only by the motion in the meridional plane. Assuming the conservation of the magnetic flux and mass, the poloidal field increases in proportional to $\rho^{2/3}$, i.e., by compression (see e.g., Ref. [37]). However, as displayed in the right-panel of Fig. 1, the central density is approximately constant during the evolution for all the models. This indicates that the increase of the poloidal-field energy is not due to the compression, but to a nonaxisymmetric effect. We will revisit this point below. We note that the internal energy is also approximately constant during the simulations, which also implies that the density distribution in the inner region of the neutron star is approximately stationary. Therefore, the magnetic field evolves passively with respect to the bulk motion inside the neutron star. This is also recognized from the left panel of Fig. 1, which shows that the profile of the

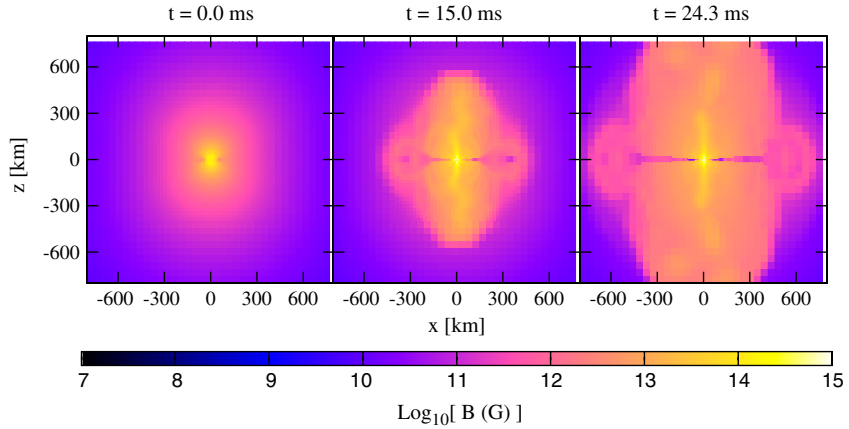

FIG. 2 (color online). Snapshots of the magnetic field strength on a meridional plane (x-z plane) at $t = 0$ ms (left), $t = 15.0$ ms (center), and $t = 24.3$ ms (right) for model B14.

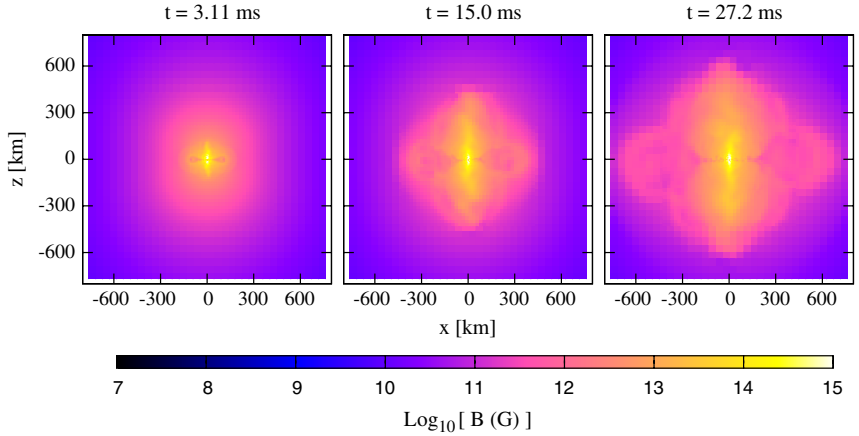

FIG. 3 (color online). The same as Fig. 2, but at $t = 3.11$ ms (left), $t = 15.0$ ms (center), and $t = 27.2$ ms (right) for model B14F.

curves of E_B for models B13 and B14 is quite similar besides the factor determined by the ratio of the initial magnetic-field strength. By contrast, the magnetic field actively evolves outside the neutron star, as described below. This active nonlinear evolution slightly modifies the scaling relation of E_B that might hold between the models of different initial magnetic-field strengths.

Figures 2 and 3 plot the snapshots of the magnetic-field strength on a meridional plane (x-z plane) at selected time slices for models B14 and B14F, respectively. The initially dipole field is distorted by the magnetic winding and consequently the strong toroidal field is generated near the rotation axis (see the central part in the middle panels of Figs. 2 and 3). Then, an outflow is driven in particular along the rotation axis (see the middle and right panels of Figs. 2 and 3). The outflow keeps blowing for a time scale much longer than the dynamical one $\sim\rho_{\rm max}^{-1/2}$ and rotation period P_c, because the strong toroidal field continues to be generated by the differential rotation in the neutron star. The asymmetry with respect to the equatorial plane develops for model B14F, which causes the less efficient winding as shown in Fig. 1. This may be also found by comparing the magnetic-field strength in the equatorial plane between two models; for model B14, the magnetic-field strength there is weak because of the symmetry imposed, whereas it is stronger for model B14F. Namely, the winding occurs less coherently for model B14F. This less coherence is likely to stem from the fact that the kink instability turns on in a stronger way in the absence of the equatorial plane symmetry (see Sec. III C). Because of this less coherence, the toroidal field grows with a longer time scale, and as a result, the head speed of the outflow for model B14F is slightly slower than that for model B14 (compare the right panels of Figs. 2 and 3).

Figure 4 plots the profiles of the magnetic field, rest-mass density, and z-component of the three velocity along the z-axis at several selected time slices for model B14. In the vicinity of the stellar polar surface, the strong magnetic field is generated and its strength reaches up to $\sim 10^{15}$ G. This substantially winded magnetic field causes a mass stripping if the magnetic pressure overcomes the gravitational binding energy density. This is approximately written by $B^2/8\pi > \rho GM/H$ where H is the vertical coordinate radius of the neutron star [36]. This is approximately equivalent to

$$v_a > v_{\rm esc}, \tag{3.6}$$

where v_a and $v_{\rm esc}$ denote the Alfvén speed and the escape velocity from the stellar surface. After the substantial winding, this condition is satisfied for a low-density surface region of the neutron star, and mass stripping turns on. Figure 4 indeed shows that near the stellar surface, $z = H \sim 10$ km, at $t = 6.01$ ms, the Alfvén speed $\sim\sqrt{B^2/(4\pi\rho)}$ is of order the speed of light, c, and hence, Eq. (3.6) is satisfied. After the mass stripping sets in, a blast

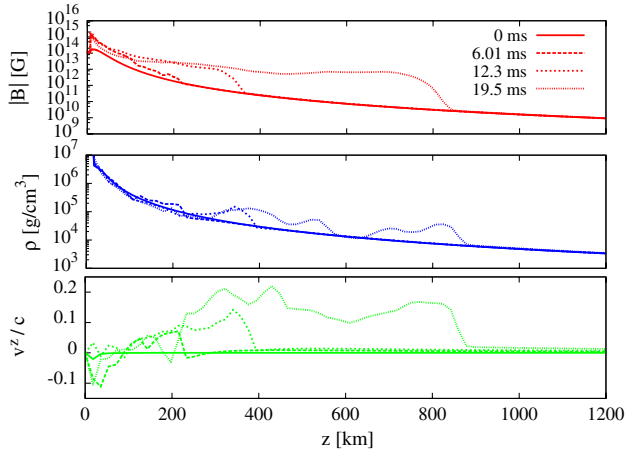

FIG. 4 (color online). Snapshots for the profiles of the magnetic field strength (top), rest-mass density (middle), and z-component of the three velocity (bottom) along the z-axis at $t = 0$ ms (solid curve), $t = 6.01$ ms (dashed curve), $t = 12.3$ ms (short-dashed curve), and $t = 19.5$ ms (dotted curve) for model B14.

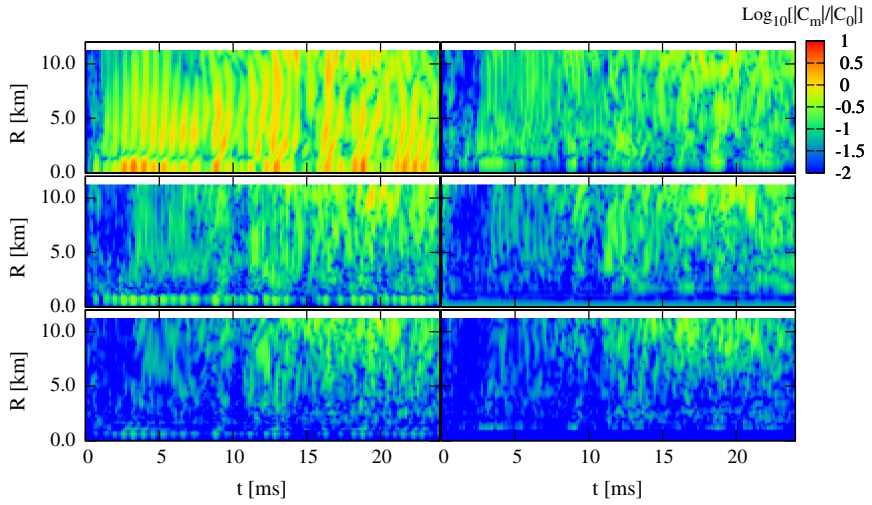

FIG. 5 (color online). Fourier mode amplitudes for the toroidal field $B_{\rm T}$ as a function of t and cylindrical coordinate R for model B14 for $m = 1$ (left-top), $m = 2$ (right-top), $m = 3$ (left-middle), $m = 4$ (right-middle), $m = 5$ (left-bottom), and $m = 6$ (right-bottom).

wave is generated, and the shock front propagates along the z-direction with its sub-relativistic head speed $\sim$0.1–0.2 c. We infer that differentially rotating magnetized neutron stars will drive the outflow as far as it is alive.

C. Kink instability

A noteworthy new feature that was not able to be found in Ref. [36] is that a nonaxisymmetric structure of the magnetic-field profile with respect to the rotation axis emerges in the outflow; see the middle and right panels in Figs. 2 and 3. This implies that a nonaxisymmetric instability sets in. This nonaxisymmetric profile is found in particular in the vicinity of the rotation axis. As already described, the strength of the toroidal field generated by the magnetic winding is as large as or larger than the poloidal-field strength in the region near the rotation axis. It is well known that a cylindrical plasma column surrounded by toroidal magnetic fields causes the kink instability [50]. The situation for the vicinity of the rotation axis is quite similar to the cylindrical plasma column. This instability is known to turn on if the following Kruskal-Shafranov (KS) instability criterion is satisfied [50]:

$$\left|\frac{B_{\rm T}}{B_{\rm P}}\right| > \frac{2\pi a}{R_0}. \tag{3.7}$$

Here, a and R_0 are the radius and poloidal extent of a cylindrical column, respectively. Because a would be smaller than $R_{\rm e}$ and $R_0 \approx z$, the condition (3.7) can be easily satisfied once the toroidal-field strength is comparable to the poloidal-field one. Hence, we infer that the magnetic outflow driven from the neutron star is subject to the kink instability.

To determine the dominant mode of the kink instability, we perform a Fourier mode analysis for the toroidal field by calculating

$$C_m(t, R, z_0) \equiv \int B_{\rm T}(t, R, \varphi, z_0) {\rm e}^{-im\varphi} d\varphi. \tag{3.8}$$

Here, the spatial hypersurface is sliced for a sequence of $z = z_0 (=$ const) planes on each of which we consider rings of radius R and perform the azimuthal integral (3.8) along the rings. Varying the radius of the rings and selected time, we plot Fig. 5 for $z_0 \approx 1.9 R_{\rm e}$. This figure shows that $m = 1$ mode turns on in particular in the vicinity of the rotation axis $R \lesssim 1$ km. We find that the ratio $|B_{\rm T}|/|B_{\rm P}| \approx 1$ at $R \approx 1$ km. The right-hand side of the KS condition (3.7) is an order of 0.1 with $a \sim 1$ km and $R_0 \sim 20$ km. Therefore, the toroidal-field strength comparable to the poloidal-field one is large enough to induce the kink instability. We find that the modes other than the $m = 1$ mode do not exhibit a remarkable growth. This implies that the $m = 1$ mode is the dominant mode, and it does not cause a strong nonlinear mode coupling.

Figure 6 plots the Fourier components of the toroidal field as functions of time, which are defined by a volume integral as

$$D_m \equiv \int B_{\rm T} {\rm e}^{-im\varphi} d^3x. \tag{3.9}$$

The left panel of Fig. 6 plots the evolution of D_m for model B14. This shows that the $m = 1$ mode is dominant among the $m = 1$–3 modes as expected from Fig. 5, and its saturation amplitude is at most $\approx$ 2–3 percents of the axisymmetric mode. This again clarifies that the nonlinearity of the kink instability is not strong enough to modify the outflow structure significantly. It should be pointed out that this weak nonlinearity was also found for the magnetic jet driven from the black hole-torus system in the simulation of Ref. [63]. The features found for model B14 also hold for other models: The right panel of Fig. 6 shows the evolution of the $m = 1$ mode for three models, showing the weak growth of the $m = 1$ mode.

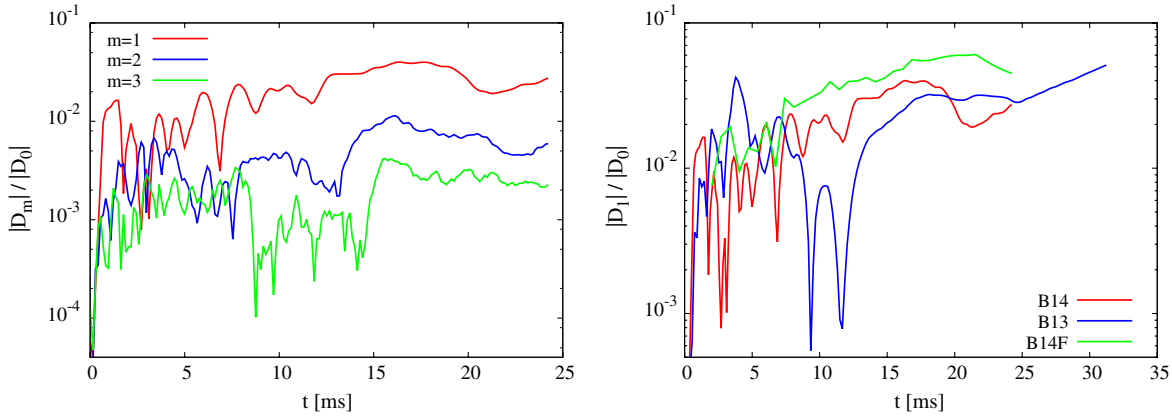

FIG. 6 (color online). Evolution of the volume integrated Fourier spectrum (a) for $m = 1$–3 modes for model B14 and (b) for $m = 1$ mode for models B13, B14, and B14F.

One point to be noted is that the saturation amplitude for model B14F is slightly larger than that of other models. The likely reason is that the absence of the equatorial-plane symmetry would enhance the growth of the kink instability (in other words, the presence of this symmetry would suppress the growth for some channel of the kink instability). The stronger excitation of the kink instability for model B14F results in a stronger modification of the axisymmetric outflow structure, which we found in Fig. 3.

D. Luminosities

The magnetic outflow driven from the magnetized neutron star is accompanied by a large amount of the ejected material and electromagnetic waves. We here define the luminosities for them by

$$L_M = -\oint_{r=\text{const}} d\theta d\varphi \sqrt{-g} (T^{(\text{mat})})^r{}_t, \tag{3.10}$$

$$L_B = -\oint_{r=\text{const}} d\theta d\varphi \sqrt{-g} (T^{(\text{em})})^r{}_t, \tag{3.11}$$

where $T^{(\text{mat})}_{\mu\nu}$ and $T^{(\text{em})}_{\mu\nu}$ are the stress energy tensor for the matter and electromagnetic field, respectively. g is the determinant of the spacetime metric. We note again that L_M includes the contribution of the rest-mass energy flow and the contribution only from the kinetic energy is by about two orders of magnitude smaller than L_M for the outflow velocity $\sim$0.1–0.2 c.

Figure 7 displays the evolution of these luminosities, which are calculated for the extraction radius of $r_{\text{ex}} \approx$ 420 km. We note that the extraction was performed for several radii and we confirmed that their luminosities depend only weakly on the extraction radii. Comparing Figs. 4 and 7, we find that for model B14, the outflow front reaches the extraction point at $t \approx 12$ ms, which corresponds to the moment of a quick rise of the luminosities. Subsequently, the order of the magnitude of the luminosities remains approximately unchanged. For other models, the feature of the luminosity curves is essentially the same. The matter energy flux for model B14 attains an order of 10^{51} erg/s. Figure 4 shows that the outflow density at the extraction point for this model is approximately 10^5 g/cm^3 and $v^z \approx 0.1$ c. These values are consistent with the matter energy flux if we assume that the matter is ejected quasi-spherically, i.e., $L_M \sim 4\pi r_{\text{ex}}^2 \rho c^2 v^z$. For the electromagnetic radiation, the luminosities for models B13 and B14 are consistent with the scaling relation (3.2), which implies that the scenario described in Ref. [36] is still valid even in the presence of the kink instability. On the other hand, the electromagnetic luminosity for model B14F is about 10 times smaller than that for model B14 at the end of the simulation. This is because the magnetic winding occurs less coherently due to a stronger effect of the kink instability, as already discussed in Sec. III C. However, during the long-term evolution, the toroidal-field energy for model B14F surpasses that for model B14 (see Fig. 1) and in

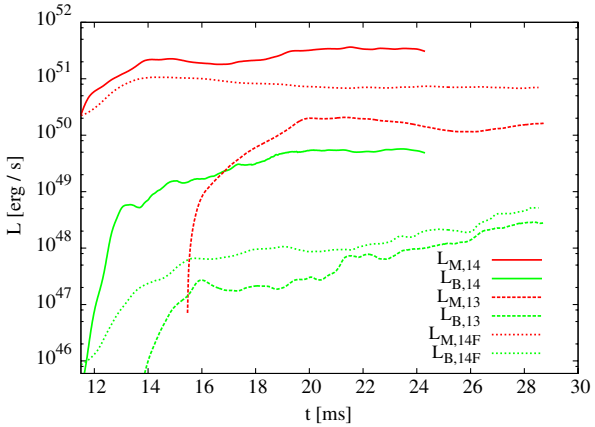

FIG. 7 (color online). Evolution of the matter and electromagnetic energy ejection rates, L_M and L_B, for three models B14, B13, and B14F, labeled by "14", "13", and "14F", respectively.

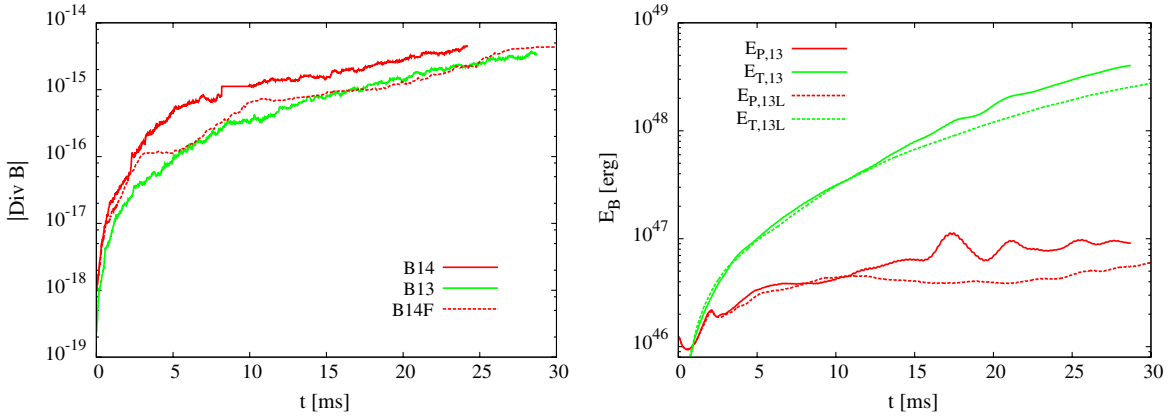

FIG. 8 (color online). Evolution of the L_∞ norm of the divergence-free condition for all the models (left) and the poloidal-field energy E_P and toroidal-field energy E_T as functions of time for models B13 and B13L (right). The right panel should be compared with the left panel of Fig. 1.

addition, Fig. 7 shows that the electromagnetic luminosity for model B14F increases gradually with time. This suggests that although the increase time scale of the toroidal-field energy and the electromagnetic luminosity is rather long, the luminosity for model B14F may be eventually as large as that for model B14.

We find that the scaling relation for the matter flux (3.1) also holds. We confirm that our result basically agrees with that in Ref. [36]. This is because the saturation amplitude of the kink instability is not large enough to disrupt the coherent toroidal magnetic-field profile, as already discussed.

E. Accuracy check

Finally, we comment on the reliability of the present simulation results. The left panel of Fig. 8 plots the magnitude of the violation for the divergence-free condition and the convergence for the evolution of E_B as functions of time. We plot the L_∞ norm of $\nabla \cdot \mathbf{B}$ for models B14, B13, and B14F. The divergence-free condition is well satisfied throughout the simulations, which means that our FMR implementation for the magnetic field works well.

The right panel of Fig. 8 plots the evolution of the magnetic-field energy for model B13 with two grid resolutions. The magnetic-field energy for both runs sufficiently converge until $t \approx 10$ ms and the poloidal-field energy starts deviating after that, although the behavior of the evolution is qualitatively the same. We attribute this loss of the convergence to the long-term accumulation of the numerical errors such as spurious magnetic reconnections due to the poor resolution. We confirmed that the qualitative features of our finding, e.g., the emergence of the kink instability and the generation of the outflow, are not affected by the grid resolution. Therefore, we conclude that the present grid setup is fine enough for obtaining scientific results for the evolution of differentially rotating magnetized neutron stars.

IV. DISCUSSION AND SUMMARY

A. Discussion

We here discuss possible electromagnetic signals emitted by the ejecta from a HMNS formed after the merger of BNS, referring to the numerical results in the present work. As mentioned in Sec. I, the recent observational result of PSR J1614-2230 suggests that the maximum mass of spherical neutron stars should be larger than $1.97 \pm 0.04 M_\odot$. This indicates that the EOS of neutron stars is stiff, and thus, a long-lived HMNS would be a canonical outcome of the BNS merger, if the binaries are composed of neutron stars of a canonical mass of 1.3–1.4$M_\odot$ with the total mass $\sim 2.7 M_\odot$ [9].

Electromagnetic signals should be emitted from the ejected material of sub-relativistic motion or ejected electromagnetic waves. According to recent studies [64–66] the ejected material will sweep up the interstellar matter and form blast waves. During this process turning on Ref. [64], the shocked material could generate magnetic fields and accelerate particles that emit synchrotron radiation, for a hypothetical amplification of the electromagnetic field and a hypothetical electron injection. The emission will peak when the total swept-up mass approaches the ejected mass, because the blast wave begins to decelerate according to a Sedov-Taylor's self-similar solution. The predicted deceleration time depends on the total energy E_0 and speed of the ejected material β_0 c as well as the number density of the interstellar matter n_0 for a single velocity outflow as [64]

$$\sim 2 \text{ yrs} \left(\frac{E_0}{10^{49} \text{ erg}}\right)^{1/3} \left(\frac{n_0}{1 \text{ cm}^{-3}}\right)^{-1/3} \left(\frac{\beta_0}{0.2}\right)^{-5/3}. \quad (4.1)$$

Here, the value of n_0 will depend strongly on the site where the merger of BNS happens. If the site is in a galactic disk, n_0 would be ~ 1 cm^{-3}, whereas if it is outside a galaxy, the value is much smaller $\sim 10^{-3}$ cm^{-3}. By the synchrotron radiation, a radio signal of ~ 0.1 GHz, which is determined

by the self-absorption, could be emitted as in the afterglow of gamma-ray bursts [64] for $n_0 \sim 1\ \mathrm{cm}^{-3}$ and $\beta = 0.2$. Then, its luminosity and flux would depend on the total kinetic energy. Figure 7 indicates that for the model with the initial maximum field strength of 10^{14} G, the luminosity of the total matter energy (including the rest mass, internal, and kinetic energies) is $\sim 10^{50}$–10^{51} erg/s. Because the typical speed of the ejected material is subrelativistic with $\beta_0 \sim 0.1$–0.2, the luminosity of the kinetic energy would be $\sim 10^{48}$–10^{49} erg/s. The latest numerical-relativity simulations indicate that the lifetime of the long-lived HMNS would be 0.1–1 s [9,11]. Thus, the predicted total kinetic energy ejected will be at most $\sim 10^{49}$ erg for $B_0 = 10^{14}$ G. If the magnetic-field strength is smaller than 10^{14} G, this value is smaller by a factor $(B_0/10^{14}\ \mathrm{G})^2$. The unabsorbed flux at the typical synchrotron frequency is

$$\sim 2.5\ \mathrm{mJy}\left(\frac{E_0}{10^{49}\ \mathrm{erg}}\right)\left(\frac{n_0}{1\ \mathrm{cm}^{-3}}\right)^{1/2}\left(\frac{\beta_0}{0.2}\right)^{-1}\times\left(\frac{D}{300\ \mathrm{Mpc}}\right)^{-2}, \tag{4.2}$$

and the peak flux at the self-absorption frequency is approximately two orders-of-magnitude smaller, i.e., $O(10)\mu$Jy level. The studies of Ref. [64] (see Table I of it) suggest that the total energy of 10^{49} erg for the subrelativistic outflow is not large enough to produce a radio signal observable by current and planned radio telescopes even for the optimistic value $n_0 = 1\ \mathrm{cm}^{-3}$ ($\sim 10^{50}$ erg is suggested to be necessary), and our estimate agrees with their results. Thus, this mass-ejection mechanism is unlikely to supply a large amount of the mass which generates a sufficiently strong radio signal, unless the magnetic-field strength is extremely large, as large as that of magnetars for which the field strength could be $\sim 10^{15}$ G.

Alternatively, the authors of Refs. [65–67] (see also Ref. [68] for the original idea) discuss the signals by the radioactive decay of r-process nuclei, which are produced from the neutron-rich material in the outflow, and subsequently decay and emit a signal that may be observable by current and planned optical telescopes such as LSST. In this scenario, the typical duration of the peak luminosity is of order a day or less as [68]

$$t_{\mathrm{peak}} \approx 0.1\mathrm{d}\left(\frac{\beta_0}{0.2}\right)^{-1/2}\left(\frac{M_{*,\mathrm{esc}}}{10^{-3}M_\odot}\right)^{1/2}, \tag{4.3}$$

and the associated peak luminosity is

$$L_{\mathrm{peak}} \approx 7\times 10^{41}\ \mathrm{erg/s}\left(\frac{f}{3\times 10^{-6}}\right)\times\left(\frac{\beta_0}{0.2}\right)^{1/2}\left(\frac{M_{*,\mathrm{esc}}}{10^{-3}M_\odot}\right)^{1/2}, \tag{4.4}$$

where $M_{*,\mathrm{esc}}$ is the total amount of the rest mass ejected and f denotes the conversion rate of the energy per rest-mass energy in the ejected material through the radioactive decay process, which is $\sim 3\times 10^{-6}$ according to the results of Ref. [65]. According to Refs. [65,66], if the total ejected mass is $\gtrsim 10^{-3}M_\odot$, the signal can be detected by large optical surveys. Figure 7 indicates that the mass ejection rate is $\sim 10^{-4}$–$10^{-3}M_\odot$/s for the maximum field strength of 10^{14} G. Thus, even if the lifetime of the HMNS is 1 s, total amount of the rest mass ejected will be $\sim 10^{-4}$–$10^{-3}M_\odot$ for this field strength. Again, unless the magnetic-field strength of the HMNS is extremely large (as large as that of magnetars), the HMNS will not eject the material which subsequently can be detected by current and planned optical telescopes.

It should be noted that our estimation is based on the magnetically driven outflow. BNS will eject a large amount of mass (10^{-3}–$10^{-2}M_\odot$) with the velocity 0.2–0.3 c through the dynamical torque that works during the merger process [69]. Such a material will be also composed primarily of neutrons and produce an amount of unstable r-process nuclei, which subsequently decay and emit a signal that may be observable by current and planned optical telescopes [65]. The large amount of the ejected materials may also contribute to generate radio signals interacting with the interstellar matter, as argued in Ref. [64].

Most important finding in the previous [36] and present works is that electromagnetic waves are emitted from the HMNS together with the mass ejection. This implies that even in the absence of the generation of blast waves via the interaction with the interstellar material, a strong magnetic field is generated. We find that the electromagnetic luminosity is 10^{49}–10^{50} erg/s for the model of the maximum field strength of 10^{14} G. For the hypothetical lifetime of the HMNS of 0.1–1 s, the total radiated energy by electromagnetic waves is $\sim 10^{49}$ erg, which is larger than the total kinetic energy of the ejected material in our model. Such huge magnetic energy, composed primarily of Alfvén waves, may be reprocessed efficiently to an observable signal as in the solar corona, although the mechanism is not clear. To clarify this point, a first-principle simulation taking into account detailed physical processes, as done, e.g., in Ref. [70] for the solar corona problem, will be necessary.

Finally, we should comment on the saturation of magnetic field strength. As shown in Fig. 1, the magnetic field continues to grow at the end of the simulation for all the models. The magnetic field strength would saturate if the magnetic field energy is as large as the kinetic energy or the thermal energy of the HMNS. We estimate the kinetic energy as $\sim 10^{53}$ erg and growth rate of the magnetic field energy in Fig. 1 as $\sim 10^{49}$ erg/ms, where we assume the toroidal magnetic field energy continues to grow by the magnetic winding and use model B14F as a representative model. Then, the magnetic field would saturate at $t \sim 100$ ms, which is shorter than the lifetime of the *HMNS* ~ 1 s. Therefore, our scaling relation (3.1) and (3.2) would breakdown after the saturation and

observational signature might be altered after that. On the other hand, if the initial magnetic field of HMNS is not strong, e.g., 10^{13} G, or the HMNS lifetime is O(0.1) s, the magnetic field strength continues to increase and the HMNS would collapse to a black hole before the magnetic field saturate and Eqs. (3.1) and (3.2) would hold.

B. Summary

Using a new GRMHD code implementing the FMR algorithm based on the divergence-free interpolation scheme of Balsara [48], we performed numerical simulations for the evolution of a differentially rotating magnetized neutron star, as an extension of our previous axisymmetric work [36]. The magnetic winding mechanism generates the strong toroidal field in particular in the vicinity of the rotation axis, as in the axisymmetric case. Subsequently, Alfvén waves propagate primarily toward the z-direction along the rotation axis and transport the electromagnetic energy. After substantial winding, the magnetic pressure overcomes the gravitational binding energy density and drives a sub-relativistic outflow. We found that in this tower-type outflow, the kink instability develops due to the presence of a strong toroidal magnetic field, and modifies the structure of the outflow that would have an axisymmetric structure in the absence of this instability. However, this instability saturates in a relatively small amplitude level, and thus, does not significantly modify the profile of the outflow. We also confirmed that the scaling relations for the matter and Poynting luminosities (3.1) and (3.2), originally found in Ref. [36], hold in the nonaxisymmetric situation as well.

As mentioned for several times in this paper, the recent observation of PSR J1614-2230 suggests that the maximum mass of spherical neutron star has to be larger than $1.97 \pm 0.04 M_\odot$, and implies that a long-lived HMNS is likely to be a canonical product of the BNS merger if the binaries are composed of neutron stars with a canonical mass of 1.3–1.4$M_\odot$ [9]. In the formed HMNS, a magnetic field will be amplified not only by the magnetic winding but also by the MRI. The MRI could cause an efficient angular momentum transport. If the strong self-gravity of a HMNS is supported primarily by its rapid rotation, the angular momentum transport could induce the collapse of the HMNS to a black hole surrounded by an accretion torus. (This is not the case if a HMNS is supported mainly by a thermal pressure [11]). The black hole-torus system formed in this scenario is a promising candidate of a central engine of short gamma-ray bursts [29,30,41,71]. We also plan to explore this scenario in the future. The most self-consistent approach for the study of these scenarios is to simulate the merger of magnetized BNS taking into account a plausible EOS for a long time from the late inspiral to the long-term evolution of the formed HMNS. We also plan to perform this type of the simulations in the future.

ACKNOWLEDGMENTS

We thank K. Hotokezaka, Y. Sekiguchi, and Y. Suwa for helpful discussions about the possible signals emitted from the outflow. K. K. also thanks T. Muranushi for a valuable comment. Numerical simulations were performed on SR16000 at YITP of Kyoto University, and XT4 at CfCA of NAOJ. This work was supported by the Grant-in-Aid for Scientific Research (21340051, 21684014, 24244028, 24740163), Scientific Research on Innovative Area (20105004), and HPCI Stragetic Program of Japanese MEXT.

APPENDIX A: CODE DESCRIPTION

In this appendix, we describe our integration scheme for the induction equation and our implementation of the FMR algorithm in details. Following Ref. [28], we choose the three magnetic field $\boldsymbol{B}^\mu \equiv \sqrt{\gamma} n_\nu F^{*\nu\mu}$ as the basic variable where $F^{*\nu\mu}$ is the dual of the Faraday tensor. This magnetic field is purely spatial in the sense that $n_\mu \boldsymbol{B}^\mu = 0$. Assuming that the ideal MHD condition holds, Maxwell's equation is recasted into the divergence-free condition and induction equation:

$$\partial_a \boldsymbol{B}^a = 0 \tag{A1}$$

$$\partial_t \boldsymbol{B}^a = \partial_b [(\boldsymbol{B}^b \boldsymbol{v}^a - \boldsymbol{B}^a \boldsymbol{v}^b)], \tag{A2}$$

where $\boldsymbol{v}^a = u^a/u^0$. We define the corresponding electric field by

$$\begin{aligned} \boldsymbol{E}_x &= -\boldsymbol{v}^y \boldsymbol{B}^z + \boldsymbol{v}^z \boldsymbol{B}^y \\ \boldsymbol{E}_y &= -\boldsymbol{v}^z \boldsymbol{B}^x + \boldsymbol{v}^x \boldsymbol{B}^z \\ \boldsymbol{E}_z &= -\boldsymbol{v}^x \boldsymbol{B}^y + \boldsymbol{v}^y \boldsymbol{B}^x. \end{aligned} \tag{A3}$$

Here, the electric field is related to the flux of the induction equation by $-\boldsymbol{B}^b \boldsymbol{v}^a + \boldsymbol{B}^a \boldsymbol{v}^b = e^{abc} \boldsymbol{E}_c$ with e^{abc} being the completely antisymmetric symbol in the flat space satisfying $e^{xyz} = 1$. In the following, we do not distinguish $\boldsymbol{E}^a$ and $\boldsymbol{E}_a$.

1. Staggered cell

The most popular and robust finite volume method to integrate ideal MHD equations is the constrained-transport scheme [58]. In this scheme, a cell for the numerical computation is defined so that fluid variables are placed in the cell center. Then, the (surface averaged) magnetic field and electric field, which is calculated from the magnetic field and velocity field, are placed on the cell surfaces and cell edges, respectively, to preserve the divergence-free condition during the evolution of the magnetic field. This prescription is compatible with an AMR or FMR implementation of Balsara [48], if the cell-centered grid is employed. For this case, the cell surface of a parent domain always agrees with the cell surfaces of its child domains, and it becomes straightforward to guarantee that

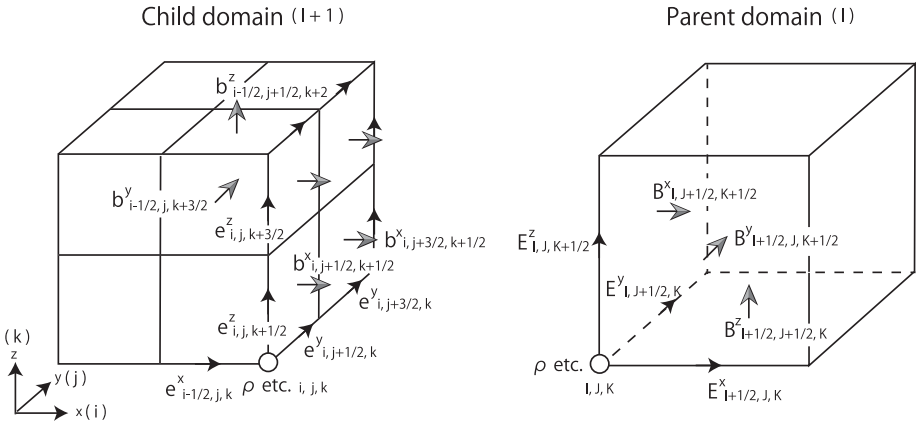

FIG. 9. Schematic picture for the structure of the cells in our FMR algorithm together with the assigned locations for the magnetic field in a child domain (left) and in a parent domain (right). Geometrical and fluid variables are defined at the cell corner, magnetic field on the cell surface, and flux at the cell edge, respectively.

the magnetic flux penetrating a surface in a parent-domain's cell agrees with the sum of the magnetic fluxes penetrating the corresponding surfaces in children-domain's cells.

However, as mentioned in Sec. II A, our code is designed for the vertex-centered grid, because it is suited for integrating Einstein's equations. This implies that the magnetic field should be placed at each cell in a different way so that surfaces of defining the magnetic field in a parent domain agree with surfaces of its child domains. Specifically, we define cells and place the magnetic field, as Fig. 9 shows. Because the vertex-centered grid is employed, the geometric and fluid variables are placed at the cell corner (i.e., at the grid). We label each grid by (i, j, k) for the child domain and by (I, J, K) for the parent domain. Then, the magnetic field is placed on the cell surface, labeled by $(i \pm 1/2, j \pm 1/2, k)$, $(i, j \pm 1/2, k \pm 1/2)$, and $(i \pm 1/2, j, k \pm 1/2)$ for the child cell. The magnetic field is defined in the range of $[-(N+1/2)\Delta x_l, (N+1/2)\Delta x_l]$. The CT scheme requires the flux (electric field) to be placed at the cell edge, labeled by $(i \pm 1/2, j, k)$, $(i, j \pm 1/2, k)$, and $(i, j, k \pm 1/2)$ for the child cell. In the following, big letters such as B^x and E^x denote the components of $\boldsymbol{B}^a$ and $\boldsymbol{E}_a$ in the parent domain, and small letters such as b^x and e^x do those in the child domain.

The parent cell contains the eight child cells and the surfaces of the parent cells always overlap with some cell surfaces of the child domain. This grid structure is essential for guaranteeing the divergence-free condition and the magnetic-flux conservation. Table III summarizes the locations where the magnetic and electric fields are defined. Then, Eq. (A2) is discretized straightforwardly as

$$\begin{aligned}
\partial_t (B^x)_{I,J+\frac{1}{2},K+\frac{1}{2}} &= -\frac{(E^z)_{I,J+1,K+\frac{1}{2}} - (E^z)_{I,J,K+\frac{1}{2}}}{\Delta y_l} + \frac{(E^y)_{I,J+\frac{1}{2},K+1} - (E^y)_{I,J+\frac{1}{2},K}}{\Delta z_l}, \\
\partial_t (B^y)_{I+\frac{1}{2},J,K+\frac{1}{2}} &= -\frac{(E^x)_{I+\frac{1}{2},J,K+1} - (E^x)_{I+\frac{1}{2},J,K}}{\Delta z_l} + \frac{(E^z)_{I+1,J,K+\frac{1}{2}} - (E^z)_{I,J,K+\frac{1}{2}}}{\Delta x_l}, \\
\partial_t (B^z)_{I+\frac{1}{2},J+\frac{1}{2},K} &= -\frac{(E^y)_{I+1,J+\frac{1}{2},K} - (E^y)_{I,J+\frac{1}{2},K}}{\Delta x_l} + \frac{(E^x)_{I+\frac{1}{2},J+1,K} - (E^x)_{I+\frac{1}{2},J,K}}{\Delta y_l},
\end{aligned} \tag{A4}$$

where $(\Delta x_l, \Delta y_l, \Delta z_l)$ denote the grid spacing for (x, y, z) in the parent level labeled by l.

According to Refs. [28,72], the electric field is computed at the cell edge by the Lax-Friedrichs formula, given by

$$\begin{aligned}
E^x = &\frac{(E^x)^{LL} + (E^x)^{LR} + (E^x)^{RL} + (E^x)^{RR}}{4} \\
&+ \frac{c_y}{2}(B_R^z - B_L^z) - \frac{c_z}{2}(B_R^y - B_L^y),
\end{aligned} \tag{A5}$$

at $(I + 1/2, J, K)$. To evaluate the flux, the magnetic field defined on the cell surface should be interpolated to the cell edge where the electric field is defined (see Fig. 9). This

TABLE III. Grid points where the geometrical and fluid variables, the magnetic field, and the electric field are defined, respectively.

Metric and fluid variables	(I, J, K)
B^x	$(I, J+\frac{1}{2}, K+\frac{1}{2})$
B^y	$(I+\frac{1}{2}, J, K+\frac{1}{2})$
B^z	$(I+\frac{1}{2}, J+\frac{1}{2}, K)$
E^x	$(I+\frac{1}{2}, J, K)$
E^y	$(I, J+\frac{1}{2}, K)$
E^z	$(I, J, K+\frac{1}{2})$

means that the magnetic field has the reconstructed right and left state. According to the prescription of the central scheme [56], we need an offset based on the characteristic speed in the flux. In the above equation, $(E^x)^{RL}$ represents the reconstructed right state in the y-direction and left state in the z-direction. The other symbols $(E^x)^{LL}$, $(E^x)^{LR}$, and $(E^x)^{RR}$ are interpreted in the similar way. (B^y_R, B^y_L) and (B^z_R, B^z_L) also denote the right and left state of $\boldsymbol{B}^y$ and $\boldsymbol{B}^z$ reconstructed. c_y and c_z are the characteristic speeds in the prescription of the upwind flux construction and calculated at cell edges with the interpolated variables. We simply calculate these quantities by averaging:

$$(c_y)_{I+\frac{1}{2},J,K} = \frac{(v^y)_{I,J,K} + (v^y)_{I+1,J,K}}{2}$$
$$(c_z)_{I+\frac{1}{2},J,K} = \frac{(v^z)_{I,J,K} + (v^z)_{I+1,J,K}}{2}. \tag{A6}$$

The formula for E^y (E^z) is obtained from Eq. (A5) by the permutation of the indices $x \to y$, $y \to z$, and $z \to x$ ($x \to z$, $y \to x$, and $z \to y$).

For solving GRMHD equations and Einstein's equations, one needs the magnetic field defined at (I, J, K). This is done by a simple averaging as

$$(B^x)_{I,J,K} = \frac{1}{4}[(B^x)_{I,J+\frac{1}{2},K+\frac{1}{2}} + (B^x)_{I,J-\frac{1}{2},K+\frac{1}{2}} + (B^x)_{I,J+\frac{1}{2},K-\frac{1}{2}} + (B^x)_{I,J-\frac{1}{2},K-\frac{1}{2}}]$$
$$(B^y)_{I,J,K} = \frac{1}{4}[(B^y)_{I+\frac{1}{2},J,K+\frac{1}{2}} + (B^y)_{I+\frac{1}{2},J,K-\frac{1}{2}} + (B^y)_{I-\frac{1}{2},J,K+\frac{1}{2}} + (B^y)_{I-\frac{1}{2},J,K-\frac{1}{2}}] \tag{A7}$$
$$(B^z)_{I,J,K} = \frac{1}{4}[(B^z)_{I+\frac{1}{2},J+\frac{1}{2},I} + (B^z)_{I-\frac{1}{2},J+\frac{1}{2},K} + (B^z)_{I+\frac{1}{2},J-\frac{1}{2},K} + (B^z)_{I-\frac{1}{2},J-\frac{1}{2},K}].$$

2. FMR implementation

For the assignment method of the variables in the interior of a cell described in Sec. A 1, we exploit the divergence-free reconstruction scheme in the refinement boundaries of the FMR algorithm, following Refs. [48,49]. First, we review how to reconstruct the magnetic field in the whole region of a cell in this scheme.

Consider a cell defined for a domain composed of $x \in [x_I, x_{I+1}]$, $y \in [y_J, y_{J+1}]$, and $z \in [z_K, z_{K+1}]$ at a FMR level l. In the first step, the magnetic-field profile on the cell surfaces are reconstructed. When we design a third-order accurate code for the spatial direction, the profile of the magnetic field, say $\tilde{B}^x$, on the surface at $x = x_I$, $y \in [y_J, y_{J+1}]$, $z \in [z_K, z_{K+1}]$ should be written as

$$\tilde{B}^x(x = x_I, y, z) = B^x_0 + B^x_y P_1(y) + B^x_z P_1(z) + B^x_{yy} P_2(y) + B^x_{yz} P_1(y) P_1(z) + B^x_{zz} P_2(z), \tag{A8}$$

where $P_1(y) = y - y_{J+1/2}$ and $P_2(y) = (y - y_{J+1/2})^2 - \Delta y_l^2/12$. We employ the WENO5 scheme to obtain the coefficients B^x_0, B^x_y, B^x_z, B^x_{yy}, B^x_{yz}, and B^x_{zz} [49]. In this scheme, we first consider the one-dimensional reconstruction problem in a zone centered at $y = y_{J+1/2}$, taking into account five neighboring variables $\{(B^x)_{J-3/2}, (B^x)_{J-1/2}, (B^x)_{J+1/2}, (B^x)_{J+3/2}, (B^x)_{J+5/2}\}$, where we omit the index I and K. Then, a third-order reconstruction over the zone centered at $y_{J+1/2}$ can be carried out by using three stencils S_1, S_2 and S_3 that rely on the variables $\{(B^x)_{J-3/2}, (B^x)_{J-1/2}, (B^x)_{J+1/2}\}$, $\{(B^x)_{J-1/2}, (B^x)_{J+1/2}, (B^x)_{J+3/2}\}$, and $\{(B^x)_{J+1/2}, (B^x)_{J+3/2}, (B^x)_{J+5/2}\}$, respectively. Because the reconstructed polynomial in the y-direction has the form

$$B^x(y) = B^x_0 + B^x_y P_1(y) + B^x_{yy} P_2(y),$$

we should calculate B^x_y and B^x_{yy} for the each stencil in the following manner;

$$(B^x_y)^{(1)} = \frac{3(B^x)_{J+1/2} - 4(B^x)_{J-1/2} + (B^x)_{J-3/2}}{2\Delta y_l}$$
$$(B^x_{yy})^{(1)} = \frac{(B^x)_{J+1/2} - 2(B^x)_{J-1/2} + (B^x)_{J-3/2}}{2\Delta y_l^2}, \tag{A9}$$

for the stencil S_1,

$$(B^x_y)^{(2)} = \frac{(B^x)_{J+3/2} - (B^x)_{J-1/2}}{2\Delta y_l}$$
$$(B^x_{yy})^{(2)} = \frac{(B^x)_{J+3/2} - 2(B^x)_{J+1/2} + (B^x)_{J-1/2}}{2\Delta y_l^2}, \tag{A10}$$

for the stencil S_2, and

$$(B^x_y)^{(3)} = \frac{-(B^x)_{J+5/2} + 4(B^x)_{J+3/2} - 3(B^x)_{J+1/2}}{2\Delta y_l}$$
$$(B^x_{yy})^{(3)} = \frac{(B^x)_{J+5/2} - 2(B^x)_{J+3/2} + (B^x)_{J+1/2}}{2\Delta y_l^2}, \tag{A11}$$

for the stencil S_3, respectively. According to the prescription in Ref. [61], we calculate the weight $\omega^{(k)}$ for each stencil with $k = 1$, 2, and 3. Then, we evaluate the coefficients as

$$B^x_y = \omega^{(1)}(B^x_y)^{(1)} + \omega^{(2)}(B^x_y)^{(2)} + \omega^{(3)}(B^x_y)^{(3)}$$
$$B^x_{yy} = \omega^{(1)}(B^x_{yy})^{(1)} + \omega^{(2)}(B^x_{yy})^{(2)} + \omega^{(3)}(B^x_{yy})^{(3)}. \tag{A12}$$

The weight $\omega^{(k)}$ is reduced to be nearly zero if the stencil k contains a discontinuity, while, for the smooth profile, it is reduced to be the optimal weight, with which the

right-hand side of Eq. (A12) can be a fifth-order accurate expression of the derivative. The coefficients B^x_z and B^x_{zz} as well as the cross term B^x_{yz} are obtained in the similar way.

Essentially the same procedure is applied to the surface at $x = x_{I+1}$. To reconstruct $\tilde{B}^y$ ($\tilde{B}^z$), the permutation rule of $x \to y$, $y \to z$, and $z \to x$ ($x \to z$, $y \to x$, and $z \to y$) should be simply applied to.

Second, we reconstruct the magnetic field in the interior of the cell, for which the third-order accurate form is

$$\begin{aligned}\hat{B}^x(x,y,z) = {} & a^x_0 + a^x_x P_1(x) + a^x_y P_1(y) + a^x_z P_1(z) + a^x_{xx} P_2(x) + a^x_{xy} P_1(x)P_1(y) + a^x_{xz} P_1(x)P_1(z) + a^x_{yy} P_2(y) \\ & + a^x_{yz} P_1(y)P_1(z) + a^x_{zz} P_2(z) + a^x_{xxx} P_3(x) + a^x_{xxy} P_2(x)P_1(y) + a^x_{xxz} P_2(x)P_1(z) + a^x_{xyy} P_1(x)P_2(y) \\ & + a^x_{xzz} P_1(x)P_2(z) + a^x_{xyz} P_1(x)P_1(y)P_1(z), \end{aligned} \tag{A13}$$

where $P_3(x) = (x - x_{I+1/2})^3 - 3(x - x_{I+1/2})\Delta x_l^2/20$. The expression for $\hat{B}^y(x,y,z)$ ($\hat{B}^z(x,y,z)$) is also obtained from the permutation of $x \to y$, $y \to z$, and $z \to x$ ($x \to z$, $y \to x$, and $z \to y$). Hence, we have to determine in total 48 unknown coefficients. Imposing that $\partial_a \boldsymbol{B}^a = 0$ holds everywhere inside the cell, we obtain 10 algebraic equations. Furthermore, we require that the profile for the interior of the cell matches that on the cell surfaces. Then, 36 algebraic equations are obtained. These 46 algebraic equations are not independent, i.e., one of them can be derived from the others. This implies that there are three degrees of freedom. We fix these degrees of freedom in the following manner: Consider one of the algebraic equations

$$a^x_{xxy} + a^y_{xyy} = -\frac{a^z_{xyz}}{2}, \tag{A14}$$

where $a^y_{xyy}(a^z_{xyz})$ is a coefficient in $\hat{B}^y(x,y,z)(\hat{B}^z(x,y,z))$ in the analogy with Eq. (A13). a^z_{xyz} can be determined by the matching at the cell surface and in the interior, and there is no equation to determine a^x_{xxy} and a^y_{xyy} other than Eq. (A14). We follow Ref. [48] to determine these coefficients. By minimizing the magnetic energy involved in the cell with respect to a^x_{xxy} and a^y_{xyy}, we obtain

$$a^x_{xxy} = a^y_{xyy} = -\frac{a^z_{xyz}}{4};$$

(see Ref. [48] in details). The same procedure is applied to the coefficients with the permutation of $x \to y$, $y \to z$, and $z \to x$, and $x \to z$, $y \to x$, and $z \to y$. As a result, three degrees of freedom are fixed.

Finally, using the algebraic equation (A13) that holds in the whole interior of the parent cell, the magnetic fields in the eight cells of the child domain $l+1$, contained within the parent cell l, are reconstructed. Because the algebraic form of the magnetic field satisfies the divergence-free condition, the magnetic field in the child cells thus determined satisfies this condition automatically.

The restriction of the magnetic field from the child cells to their parent cell is done at specific time step levels: We choose the time-step levels in the FMR algorithm following Refs. [6,73]. Specifically, the time step intervals for each FMR level is chosen by

$$\Delta t_l = \begin{cases} c_{\rm CFL}\Delta x_{l_c} & \text{for } 1 \le l \le l_c, \\ c_{\rm CFL}\Delta x_l & \text{for } l_c < l \le l_{\rm max}, \end{cases} \tag{A15}$$

where $c_{\rm CFL}$ is the Courant number ≈ 0.4–0.5. Namely, for the coarser levels with $l \le l_c$, the time step intervals are chosen to be identical while it is chosen to be proportional to the grid spacing for $l > l_c$ (see Fig. 10). In this setup, the restriction is done when the time slice of the child domain agrees with that of the corresponding parent domain (see the time step level $n+1$ in Fig. 10). The simplest form for the restriction would be (cf., Fig. 9)

$$\begin{aligned}(B^x)_{I,J+\frac{1}{2},K+\frac{1}{2}} = \frac{1}{4}(& b^x_{i,j+\frac{1}{2},k+\frac{1}{2}} + b^x_{i,j+\frac{3}{2},k+\frac{1}{2}} \\ & + b^x_{i,j+\frac{1}{2},k+\frac{3}{2}} + b^x_{i,j+\frac{3}{2},k+\frac{3}{2}}). \end{aligned} \tag{A16}$$

However, this cannot be employed, because the divergence-free condition is not satisfied in the parent level: Note that the divergence-free condition for B^a is preserved if the flux calculated from the electric field E^a is used to integrate the induction equation. However, in the restriction (A16), e^y and e^z, instead of E^y and E^z, are used to update B^x (cf., Fig. 9). For such cases, simple restriction schemes in general do not work well.

Thus, following Ref. [48], we add a correction in addition to the "zeroth-order" restriction (A16), to preserve the divergence-free condition of the magnetic field. Reference [48] proposed to use the following restriction: For $l > l_c$

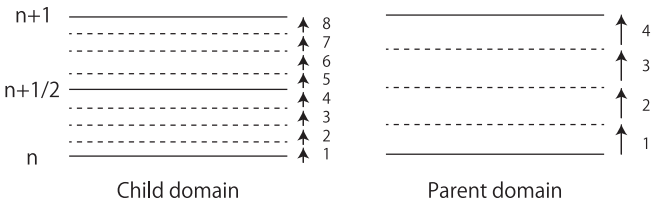

FIG. 10. Schematic picture of the time integration scheme for a child domain of label $l+1$ (left) and parent domain of label l from n to $n+1$ time slice for the domain $l > l_c$. Attached small arrows with numbers denote the sub-step for the fourth-order Runge-Kutta integration.

TABLE IV. Initial data and grid setup for 1D MHD tests. Initial states are separated in the left ($x < 0$) and right ($x > 0$) state with a discontinuity at $x = 0$. $2N + 1$ and $l_{\max}$ denote the number of the grid point covering the interval $[-N\Delta x_l, N\Delta x_l]$ in a FMR domain and the number of FMR domains, respectively.

Test	Left state ($x < 0$)	Right state ($x > 0$)	$t_{\rm fin}$	$\Delta x_{l_{\max}}$	N	$l_{\max}$
Fast Shock	$u^a = (25.0, 0.0, 0.0)$	$u^a = (1.091, 0.3923, 0.00)$	4.9	0.005	204	2
	$B^a/\sqrt{4\pi} = (20.0, 25.02, 0.0)$	$B^a/\sqrt{4\pi} = (20.0, 49.0, 0.0)$				
	$P = 1.0$, $\rho = 1.0$	$P = 367.5$, $\rho = 25.48$				
Slow Shock	$u^a = (1.53, 0.0, 0.0)$	$u^a = (0.9571, -0.6822, 0.00)$	2.0	0.005	204	2
	$B^a/\sqrt{4\pi} = (10.0, 18.28, 0.0)$	$B^a/\sqrt{4\pi} = (10.0, 14.49, 0.0)$				
	$P = 10.0$, $\rho = 1.0$	$P = 55.36$, $\rho = 3.323$				
Switch-off	$u^a = (-2.0, 0.0, 0.0)$	$u^a = (-0.212, -0.590, 0.0)$	1.8	0.005	204	2
Fast Rarefaction	$B^a/\sqrt{4\pi} = (2.0, 0.0, 0.0)$	$B^a/\sqrt{4\pi} = (2.0, 4.71, 0.0)$				
	$P = 1.0$, $\rho = 0.1$	$P = 10.0$, $\rho = 0.562$				
Switch-on	$u^a = (-0.765, -1.386, 0.0)$	$u^a = (0.0, 0.0, 0.0)$	2.2	0.005	204	2
Fast Rarefaction	$B^a/\sqrt{4\pi} = (1.0, 1.022, 0.0)$	$B^a/\sqrt{4\pi} = (1.0, 0.0, 0.0)$				
	$P = 0.1$, $\rho = 1.78 \times 10^{-3}$	$P = 1.0$, $\rho = 0.01$				
Shock Tube 1	$u^a = (0.0, 0.0, 0.0)$	$u^a = (0.0, 0.0, 0.0)$	2.2	0.005	204	2
	$B^a/\sqrt{4\pi} = (1.0, 0.0, 0.0)$	$B^a/\sqrt{4\pi} = (1.0, 0.0, 0.0)$				
	$P = 1000.0$, $\rho = 1.0$	$P = 1.0$, $\rho = 0.1$				
Shock Tube 2	$u^a = (0.0, 0.0, 0.0)$	$u^a = (0.0, 0.0, 0.0)$	2.3	0.005	204	2
	$B^a/\sqrt{4\pi} = (0.0, 0.20, 0.0)$	$B^a/\sqrt{4\pi} = (0.0, 0.0, 0.0)$				
	$P = 30.0$, $\rho = 1.0$	$P = 1.0$, $\rho = 0.1$				

$$
\begin{aligned}
(B^y)_{I+\frac{1}{2},J,K+\frac{1}{2}} &\to (B^y)_{I+\frac{1}{2},J,K+\frac{1}{2}} + \sum_{m=1}^{4} \Delta t_l^{(m)} \frac{(E^z)^{(m)}_{I,J,K+\frac{1}{2}}}{\Delta x_l} - \frac{1}{4} \sum_{m=1}^{8} \Delta t_{l+1}^{(m)} \frac{(e^z)^{(m)}_{i,j,k+\frac{1}{2}} + (e^z)^{(m)}_{i,j,k+\frac{3}{2}}}{\Delta x_{l+1}}, \\
(B^y)_{I+\frac{1}{2},J+1,K+\frac{1}{2}} &\to (B^y)_{I+\frac{1}{2},J+1,K+\frac{1}{2}} + \sum_{m=1}^{4} \Delta t_l^{(m)} \frac{(E^z)^{(m)}_{I,J+1,K+\frac{1}{2}}}{\Delta x_l} - \frac{1}{4} \sum_{m=1}^{8} \Delta t_{l+1}^{(m)} \frac{(e^z)^{(m)}_{i,j+2,k+\frac{1}{2}} + (e^z)^{(m)}_{i,j+2,k+\frac{3}{2}}}{\Delta x_{l+1}}, \\
(B^z)_{I+\frac{1}{2},J+\frac{1}{2},K} &\to (B^z)_{I+\frac{1}{2},J+\frac{1}{2},K} - \sum_{m=1}^{4} \Delta t_l^{(m)} \frac{(E^y)^{(m)}_{I,J+\frac{1}{2},K}}{\Delta x_l} + \frac{1}{4} \sum_{m=1}^{8} \Delta t_{l+1}^{(m)} \frac{(e^y)^{(m)}_{i,j+\frac{1}{2},k} + (e^y)^{(m)}_{i,j+\frac{3}{2},k}}{\Delta x_{l+1}}, \\
(B^z)_{I+\frac{1}{2},J+\frac{1}{2},K+1} &\to (B^z)_{I+\frac{1}{2},J+\frac{1}{2},K+1} - \sum_{m=1}^{4} \Delta t_l^{(m)} \frac{(E^y)^{(m)}_{I,J+\frac{1}{2},K}}{\Delta x_l} + \frac{1}{4} \sum_{m=1}^{8} \Delta t_{l+1}^{(m)} \frac{(e^y)^{(m)}_{i,j+\frac{1}{2},k+2} + (e^y)^{(m)}_{i,j+\frac{3}{2},k+2}}{\Delta x_{l+1}},
\end{aligned}
\tag{A17}
$$

where the time step intervals of the Runge-Kutta integration are defined as follows: $\Delta t_{l'}^{(1)} = \Delta t_{l'}^{(4)} = \Delta t_{l'}/6$, $\Delta t_{l'}^{(2)} = \Delta t_{l'}^{(3)} = \Delta t_{l'}/3$ with $l' = l, l+1$, $\Delta t_{l+1}^{(5)} = \Delta t_{l+1}^{(8)} = \Delta t_{l+1}/6$, and $\Delta t_{l+1}^{(6)} = \Delta t_{l+1}^{(7)} = \Delta t_{l+1}/3$. $(E^y)^{(m)}$, $(E^z)^{(m)}$, $(e^y)^{(m)}$, and $(e^z)^{(m)}$ denote the electric-field components at sub-step levels, m, of the Runge-Kutta integration (see Fig. 10). For $l \le l_c$ for which the time step intervals are identical, the third term of the right-hand sides of (A17) should be replaced from $\sum_{m=1}^{8}$ to $\sum_{m=1}^{4}$. The similar procedure is applied for B^y and B^z by the permutation of the indices. These prescriptions guarantee both the magnetic-flux conservation and the preservation of the divergence-free condition.

APPENDIX B: CODE TESTS

1. One-dimensional tests

We here report the results for one-dimensional MHD tests in the Minkowski spacetime, proposed in Ref. [74]. The initial data of the tests are summarized in Table IV. For all the initial data, a discontinuity is present at $x = 0$, and the left ($x < 0$) and right ($x > 0$) states are composed of uniform profiles. For all the cases, the Γ-law EOS with $\Gamma = 4/3$ is adopted. We performed these tests in a three-dimensional code assuming that all the quantities are uniformly distributed in the y-and z-directions. The divergence-free condition of the magnetic field implies

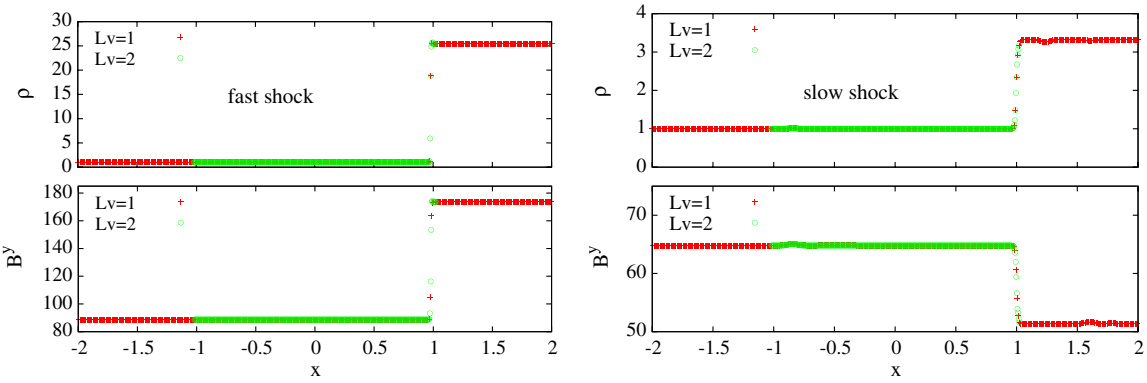

FIG. 11 (color online). Snapshots of rest-mass density and y-component of the magnetic field in 1D fast shock (left) and slow shock (right) problems. Numerical solutions are plotted both for the FMR domain 1 (cross symbol) and domain 2 (circle symbol).

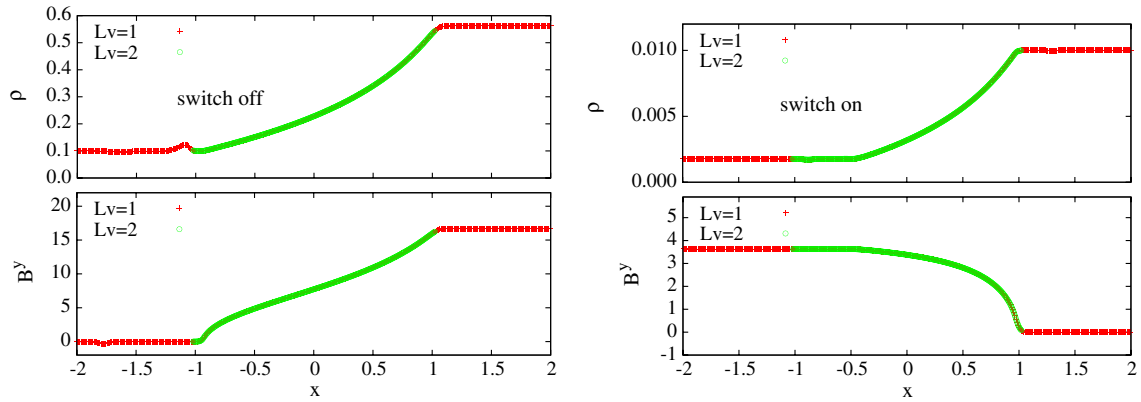

FIG. 12 (color online). The same as Fig. 11 but for the 1D switch-off and switch-on test problems.

that B^x is a constant along the x direction. Because B^x does not evolve in this test, the divergence-free condition is automatically satisfied.

The purpose of this section is to demonstrate that our FMR code works well even in the presence of discontinuities and shock waves across the refinement boundaries. To do this, we prepare a computational region composed of two FMR domains, for which the grid point and resolution are summarized in Table IV. The simulations were terminated at $t_{\rm fin}$ when a discontinuity or waves go through the refinement boundary. Figures 11–13 plot the snapshots of ρ and B^y at $t = t_{\rm fin}$. Numerical solutions in the FMR domains 1 and 2 are plotted together with the red-plus and green-circle symbols. The solutions in both domains agree approximately with the analytic solutions, except for a spurious small modulation for ρ in the region

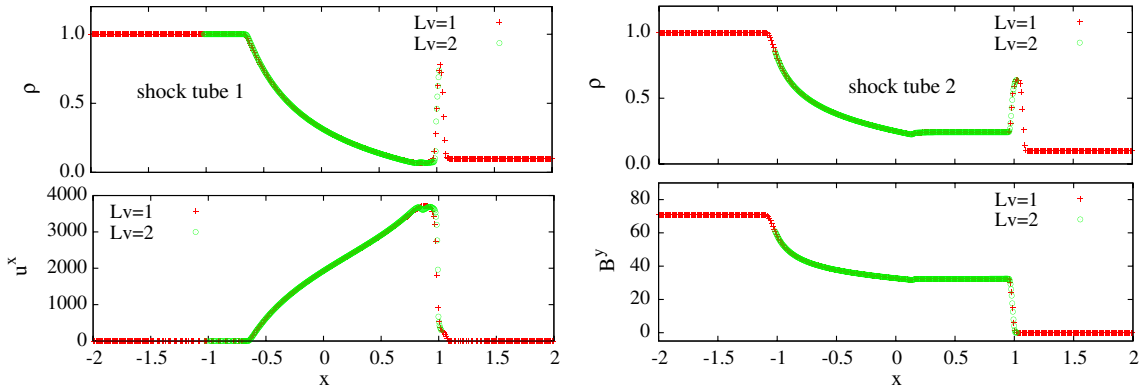

FIG. 13 (color online). The same as Fig. 11 but for the shock tube 2 tests. For the 1D shock tube 1, we plot the four velocity weighted by the enthalpy instead of the magnetic field because $B^y = 0$ in this simulation.

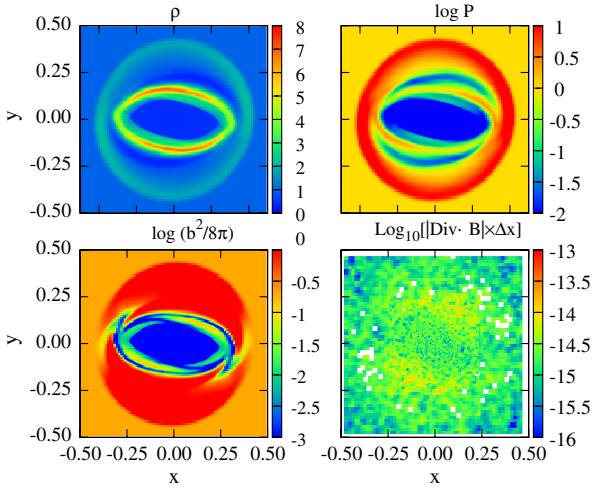

FIG. 14 (color online). The results of a cylindrically rotating disk problem: Rest-mass density ρ (top-left), pressure (top-right), magnetic field strength b^2 (bottom-left), and divergence-free condition (bottom-right) on the x-y plane at $t = 0.4$.

$1.0 \lesssim x \lesssim 1.7$ in the slow shock test and a small bump around $x = -1$ in the switch-off test. As reported in Ref. [28], these errors are generated by the initially discontinuous data at $x = 0$ irrespective of grid resolutions and presence of the FMR refinement boundary. The amplitudes of those errors are known to gradually decrease with improving the grid resolution. The point to be stressed is that the discontinuities and waves pass thorough from the domain 2 to domain 1 without any problems. These results validate the implementation of staggered magnetic fields, prolongation, and restriction described in the previous section.

2. Two-dimensional tests

We also performed a two-dimensional cylindrically rotating disk test proposed in Ref. [72]. All the variables are assumed to be functions only of x and y in this test, although the simulation was performed by a three-dimensional code. The employed initial condition was

$$(\rho, P, B^x/\sqrt{4\pi}, B^y/\sqrt{4\pi}, v^x, v^y) = \begin{cases} (10, 1, 1, 0, -\omega y, \omega x) & \text{for } (\sqrt{x^2+y^2} \le 0.1) \\ (1, 1, 1, 0, 0, 0) & \text{for } (\sqrt{x^2+y^2} \ge 0.1) \end{cases} \quad \text{(B1)}$$

with $\omega = 9.95$. In this test, we adopted the $\Gamma = 5/3$ EOS and prepared three FMR domains which are composed of squares with the regions $x, y \in [-0.512, 0.512]$ for domain 1, $x, y \in [-0.256, 0.256]$ for domain 2, and $x, y \in [-0.128, 0.128]$ for domain 3. The finest grid spacing and grid points were chosen to be 0.001 and 128, respectively, which is equivalent to the middle resolution in Ref. [46]. Comparing the result in Ref. [46], we found that all the quantities were well reproduced. The divergence-free condition was also satisfied with a high precision (see the bottom-right panel of Fig. 14). Therefore, we confirm that our FMR implementation works well.

[1] G. M. Harry (LIGO Scientific Collaboration), Classical Quantum Gravity **27**, 084006 (2010); T. Accadia *et al.*, Classical Quantum Gravity **28**, 025005 (2011); K. Kuroda *et al.*, Classical Quantum Gravity **27**, 084004 (2010); B. Willke *et al.*, Classical Quantum Gravity **23**, S207 (2006).

[2] E. Nakar, Phys. Rep. **442**, 166 (2007).

[3] M. Shibata, K. Taniguchi, and K. Uryu, Phys. Rev. D **68**, 084020 (2003).

[4] M. Shibata, K. Taniguchi, and K. Uryu, Phys. Rev. D **71**, 084021 (2005).

[5] M. Shibata and K. Taniguchi, Phys. Rev. D **73**, 064027 (2006).

[6] T. Yamamoto, M. Shibata, and K. Taniguchi, Phys. Rev. D **78**, 064054 (2008).

[7] K. Kiuchi, Y. Sekiguchi, M. Shibata, and K. Taniguchi, Phys. Rev. D **80**, 064037 (2009).

[8] K. Kiuchi, Y. Sekiguchi, M. Shibata, and K. Taniguchi, Phys. Rev. Lett. **104**, 141101 (2010).

[9] K. Hotokezaka, K. Kyutoku, H. Okawa, M. Shibata, and K. Kiuchi, Phys. Rev. D **83**, 124008 (2011).

[10] Y. Sekiguchi, K. Kiuchi, K. Kyutoku, and M. Shibata, Phys. Rev. Lett. **107**, 211101 (2011).

[11] Y. Sekiguchi, K. Kiuchi, K. Kyutoku, and M. Shibata, Phys. Rev. Lett. **107**, 051102 (2011).

[12] L. Baiotti, B. Giacomazzo, and L. Rezzolla, Phys. Rev. D **78**, 084033 (2008).

[13] L. Rezzolla, L. Baiotti, B. Giacomazzo, D. Link, and J. A. Font, Classical Quantum Gravity **27**, 114105 (2010).

[14] L. Baiotti, T. Damour, B. Giacomazzo, A. Nagar, and L. Rezzolla, Phys. Rev. D **84**, 024017 (2011).

[15] P. Marronetti, M. D. Duez, S. L. Shapiro, and T. W. Baumgarte, Phys. Rev. Lett. **92**, 141101 (2004).

[16] J. A. Faber, T. W. Baumgarte, S. L. Shapiro, and K. Taniguchi, Astrophys. J. **641**, L93 (2006).

[17] M. D. Duez, Classical Quantum Gravity **27**, 114002 (2010).

[18] M. Anderson, E. W. Hirschmann, L. Lehner, S. L. Liebling, P. M. Motl, D. Neilsen, C. Palenzuela, and J. E. Tohline, Phys. Rev. D **77**, 024006 (2008).

[19] M. Thierfelder, S. Bernuzzi, and B. Bruegmann, Phys. Rev. D **84**, 044012 (2011).

[20] M. Shibata and K. Uryu, Phys. Rev. D **61**, 064001 (2000).
[21] R. N. Manchester, G. B. Hobbs, A. Teoh, and M. Hobbs, Astron. J. **129**, 1993 (2005).
[22] S. A. Balbus and J. F. Hawley, Rev. Mod. Phys. **70**, 1 (1998).
[23] N. Bucciantini and L. Del Zanna, Astron. Astrophys. **528**, A101 (2011).
[24] T. Kuroda and H. Umeda, Astrophys. J. Suppl. Ser. **191**, 439 (2010).
[25] B. Giacomazzo and L. Rezzolla, Classical Quantum Gravity **24**, S235 (2007).
[26] S. L. Liebling, L. Lehner, D. Neilsen, and C. Palenzuela, Phys. Rev. D **81**, 124023 (2010).
[27] M. D. Duez, Y. T. Liu, S. L. Shapiro, and B. C. Stephens, Phys. Rev. D **72**, 024028 (2005).
[28] M. Shibata and Y.-i. Sekiguchi, Phys. Rev. D **72**, 044014 (2005).
[29] M. D. Duez, Y. T. Liu, S. L. Shapiro, M. Shibata, and B. C. Stephens, Phys. Rev. Lett. **96**, 031101 (2006).
[30] M. Shibata, M. D. Duez, Y. T. Liu, S. L. Shapiro, and B. C. Stephens, Phys. Rev. Lett. **96**, 031102 (2006).
[31] M. D. Duez, Y. T. Liu, S. L. Shapiro, and M. Shibata, Phys. Rev. D **73**, 104015 (2006).
[32] S. Chawla, M. Anderson, M. Besselman, L. Lehner, S. L. Liebling, P. M. Motl, and D. Neilsen, Phys. Rev. Lett. **105**, 111101 (2010).
[33] Z. B. Etienne, Y. T. Liu, V. Paschalidis, and S. L. Shapiro, Phys. Rev. D **85**, 064029 (2012).
[34] K. Kiuchi, M. Shibata, and S. Yoshida, Phys. Rev. D **78**, 024029 (2008).
[35] K. Kiuchi, S. Yoshida, and M. Shibata, Astron. Astrophys. **532**, A30 (2011).
[36] M. Shibata, Y. Suwa, K. Kiuchi, and K. Ioka, Astrophys. J. **734**, L36 (2011).
[37] M. Shibata, Y. T. Liu, S. L. Shapiro, and B. C. Stephens, Phys. Rev. D **74**, 104026 (2006).
[38] Y. T. Liu, S. L. Shapiro, Z. B. Etienne, and K. Taniguchi, Phys. Rev. D **78**, 024012 (2008).
[39] B. Giacomazzo, L. Rezzolla, and L. Baiotti, Mon. Not. R. Astron. Soc. **399**, L164 (2009).
[40] B. Giacomazzo, L. Rezzolla, and L. Baiotti, Phys. Rev. D **83**, 044014 (2011).
[41] L. Rezzolla, B. Giacomazzo, L. Baiotti, J. Granot, C. Kouveliotou, and M. A. Aloy, Astrophys. J. **732**, L6 (2011).
[42] M. Anderson, E. W. Hirschmann, L. Lehner, S. L. Liebling, P. M. Motl, D. Neilsen, C. Palenzuela, and J. E. Tohline, Phys. Rev. Lett. **100**, 191101 (2008).
[43] D. Price and S. Rosswog, Science **312**, 719 (2006).
[44] Long-lived HMNS implies that its lifetime is much longer than the dynamical time scale $\sim$1 s. For the detailed definition of the long-lived HMNS, see Ref. [9]
[45] P. Demorest, T. Pennucci, S. Ransom, M. Roberts, and J. Hessels, Nature (London) **467**, 1081 (2010).
[46] Z. B. Etienne, Y. T. Liu, and S. L. Shapiro, Phys. Rev. D **82**, 084031 (2010).
[47] Z. B. Etienne, V. Paschalidis, Y. T. Liu, and S. L. Shapiro, Phys. Rev. D **85**, 024013 (2012).
[48] D. Balsara, J. Comp. Phys. **174**, 614 (2001); J. Comp. Phys. **228**, 5040 (2009).
[49] D. Balsara, T. Rumpf, M. Dumbser, and C. Munz, J. Comp. Phys. **228**, 2480 (2009).
[50] H. Goedbloed and S. Poedts, *Principles of Magnetohydrodynamics* (Cambridge University Press, Cambridge, England, 2004).
[51] M. Shibata and T. Nakamura, Phys. Rev. D **52**, 5428 (1995).
[52] T. W. Baumgarte and S. L. Shapiro, Phys. Rev. D **59**, 024007 (1998).
[53] M. Campanelli, C. O. Lousto, P. Marronetti, and Y. Zlochower, Phys. Rev. Lett. **96**, 111101 (2006).
[54] J. G. Baker, J. Centrella, D.-I. Choi, M. Koppitz, and J. van Meter, Phys. Rev. Lett. **96**, 111102 (2006).
[55] B. Bruegmann, J. A. Gonzalez, M. Hannam, S. Husa, U. Sperhake, and W. Tichy, Phys. Rev. D **77**, 024027 (2008).
[56] A. Kruganov and E. Tadmor, J. Comput. Physiol., **160**, 241 (2000).
[57] M. Alcubierre, B. Bruegmann, P. Diener, M. Koppitz, D. Pollney, E. Seidel, and R. Takahashi, Phys. Rev. D **67**, 084023 (2003).
[58] C. R. Evans and J. F. Hawley, Astrophys. J. **332**, 659 (1988).
[59] D. Balsara and D. Spicer, J. Comp. Phys. **149**, 270 (1999).
[60] M. Anderson, E. Hirschmann, S. L. Liebling, and D. Neilsen, Classical Quantum Gravity **23**, 6503 (2006).
[61] G. Jiang and C. Shu, J. Comp. Phys. **126**, 202 (1996).
[62] Note that the MRI [22] may occur in the magnetized neutron star. However, the wavelength for the fastest growing mode is too short to be resolved by the present grid resolution: Assuming the typical value for the HMNS, the MRI wavelength is $6 \times 10^3 (B/10^{14}\ \mathrm{G}) \times (\rho/10^{15}\ \mathrm{g/cm^3})^{-1/2} (\Omega/10^3\ \mathrm{rad/s})^{-1}$ cm. Typical resolution of our simulation is an order of 10^4 cm (see Table II). If the effect of the MRI could be incorporated, we may find that the power of the outflow driven is higher than that found in the present work.
[63] J. C. McKinney and R. D. Blandford, Mon. Not. R. Astron. Soc. **394**, L126 (2009).
[64] E. Nakar and T. Piran, Nature (London) **478**, 82 (2011).
[65] B. D. Metzger, G. Martinez-Pinedo, S. Darbha, E. Quataert, A. Arcones, D. Kasen, T. Thomas, P. Nugent, I. V. Panov, and N. T. Zinner, Mon. Not. R. Astron. Soc. **406**, 2650 (2010).
[66] B. D. Metzger and E. Berger, Astrophys. J. **746**, 48 (2012).
[67] S. R. Kulkarni, arXiv:0501256.
[68] L. Li and B. Paczyński, Astrophys. J. **507**, L59 (1998).
[69] K. Hotokezaka *et al.* (unpublished).
[70] T. K. Suzuki and S. Inutsuka, Astrophys. J. **632**, L49 (2005).
[71] R. Narayan, B. Paczyński, and T. Piran, Astrophys. J. **395**, L83 (1992).
[72] L. Del Zanna, N. Bucciantini, and P. Londrillo, Astron. Astrophys. **400**, 397 (2003).
[73] M. Berger and J. Oliger, J. Comp. Phys. **53**, 484 (1984).
[74] S. S. Komissarov, Mon. Not. R. Astron. Soc. **303**, 343 (1999).